

QUANTIFYING THE EFFECT OF CONDUCTIVE
POLYMER BINDERS ON LI-O₂ BATTERY
PERFORMANCE

by
Amy J. LeBar

© Copyright by Amy J. LeBar, 2019

All Rights Reserved

A thesis submitted to the Faculty and the Board of Trustees of the Colorado School of Mines in partial fulfillment of the requirements for the degree of Master of Science (Mechanical Engineering).

Golden, Colorado

Date _____

Signed: _____
Amy J. LeBar

Signed: _____
Dr. Steven C. DeCaluwe
Thesis Advisor

Golden, Colorado

Date _____

Signed: _____
Dr. John R. Berger
Professor and Head
Department of Mechanical Engineering

ABSTRACT

Electric vehicles (EVs) have gained popularity in recent years for their ability to reduce carbon emissions. However, increased commercial adoption requires advancements in battery energy density, to enable longer drive times without significantly increasing vehicle weight. Li-O₂ batteries are a promising new energy storage technology — with a theoretical energy density of 3500 Wh/kg_{battery}, Li-O₂ batteries can enable EVs which can drive up to 1000 miles between charges. However, Li-O₂ battery development is limited by a number of fundamental challenges, which result in poor rate capabilities due to transport and surface reactions, low energy efficiency, and rapid battery degradation due to material instability.

This thesis project seeks to understand the effect of conductive polymer binders (such as Nafion) in Li-O₂ battery cathodes on battery performance. Binders are a necessary component to battery cathodes—they literally bind cathode particles together, providing for electrical conductivity and a physically coherent structure—but add weight and do not contribute directly to electrochemical activity. Moreover, binders block access to reactive surfaces and impede transport of dissolved electrolyte species through the cathode thickness, reducing battery capacity, particularly under higher currents. Lastly, side reactions between binder materials and reactive intermediates in the electrolyte contribute to battery degradation. With the addition of conductive polymer binders such as Nafion in the cathode, we expect to see improved battery performance due to enhanced transport, reactive surface areas, and material stability. However, the direct role played by novel binder materials is poorly understood.

Herein, we present combined Li-O₂ battery experiments and numerical simulations to quantify the impact of novel conductive binders on battery performance. Carbon paper was used as a model Li-O₂ cathode with limited microstructural variation, and battery cycling and electronic impedance spectroscopy data were collected for three types of cells: (i)

no binder, (ii) a non-conductive PTFE binder, (iii) and a conductive Lithiated Nafion binder. The experimental results demonstrate that the battery performance is very sensitive to the cathode microstructure—results showed significant sample-to-sample variation, presumably due to variations in the binder deposition and dispersion. These variations prevent any definitive conclusions about the impact of the conductive binders, but guide future development of cathode fabrication processes. The experimental results also demonstrate the crucial impact of microstructure and surface area in Li-O₂ battery operation. Even at very low currents, the battery charges and discharges at voltages well off from its thermodynamic equilibrium potential, demonstrating poor energy efficiency, and have capacities well below the theoretical limit. Validating a one-dimensional Li-O₂ battery model against this battery data confirms the rate-limiting nature of the surface area for these cells. Simulation results varied strongly with the available surface area but were largely insensitive to transport-related phenomena. Moreover, at these current densities, negligible property gradients through the cathode depth were observed, indicating that transport did not play a limiting role, at these conditions.

This work establishes experimental and numerical simulation routines for further Li-O₂ research into the impact of conductive polymer binders. Results demonstrate the critical role of surface area in Li-O₂ battery performance and demonstrate the infeasibility of carbon paper as a model Li-O₂ cathode. Based on these results, future research will focus on developing and refining binder dispersion routines for higher-surface area cathodes.

TABLE OF CONTENTS

ABSTRACT	iii
LIST OF FIGURES AND TABLES	viii
LIST OF ABBREVIATIONS	x
ACKNOWLEDGMENTS	xi
DEDICATION	xii
CHAPTER 1 INTRODUCTION	1
1.1 Introduction	1
1.2 Li-O ₂ Research and Development	3
1.3 Current Challenges	4
1.4 Thesis Overview	6
CHAPTER 2 EXPERIMENTAL CHARACTERIZATION OF LI-O ₂ BATTERIES	8
2.1 Introduction	8
2.2 Methods	8
2.2.1 Electrolyte preparation	9
2.2.2 Cathode preparation	9
2.2.3 Cell preparation and assembly	10
2.2.4 Cell disassembly and cleaning	12
2.3 Experimental Methods	12
2.3.1 Discharge capacity vs. cycle number	12
2.3.2 Electrochemical impedance spectroscopy	13

2.3.3	Field emission scanning electron microscopy	13
2.4	Experimental Results	14
2.4.1	Capacity vs. cycle number	14
2.4.2	Repeatability	17
2.4.3	Electrochemical impedance spectroscopy	18
2.4.4	FESEM imaging	23
2.5	Discussion	26
2.6	Conclusions	28
CHAPTER 3 1D LI-O ₂ BATTERY MODEL		29
3.1	Introduction	29
3.2	Model Framework	31
3.2.1	Governing equations	31
3.2.2	Chemical and flux terms	34
3.2.3	Electrochemical kinetics	35
3.2.4	Boundary conditions	35
3.3	Binder Effects	36
3.4	Model Fitting and Validation	37
3.5	Results	38
3.6	Discussion	41
3.7	Conclusions	43
CHAPTER 4 CONCLUSIONS		44
4.1	Summary of Efforts	44
4.2	Key Findings	45

4.3	Future Work	46
4.4	Outlook	48
	REFERENCES CITED	49
	APPENDIX CELL ASSEMBLY AND DISASSEMBLY	51
A.1	Electrolyte Preparation - 1 M LiTFSI in TEGDME	51
A.2	Cell Assembly	51
A.3	Disassembly and Cleaning	52

LIST OF FIGURES AND TABLES

Figure 1.1	Schematic of Li-O ₂ battery operation.	2
Figure 1.2	Visualization of the possible locations for Li ₂ O ₂ formation within the battery's GDL. This figure was taken from the Department of Energy funding proposal	6
Figure 2.1	Cross-sectional view of the ECC-DEMS cell	11
Figure 2.2	Electrode and gas port connections for battery cell based on EL-cell ECC-DEMS user manual	11
Figure 2.3	Charge-discharge curves for a Li-O ₂ cathode with no binder. The cell was cycled at 1 mA between 2 and 4.5 V.	15
Figure 2.4	Charge-discharge curves for a Li-O ₂ cathode with PTFE binder. The cell was cycled at 1 mA between 2 and 4.5 V.	15
Figure 2.5	Charge-discharge curves for a Li-O ₂ cathode with Nafion binder. The cell was cycled at 1 mA between 2 and 4.5 V.	16
Figure 2.6	Discharge degradation of cells without a binder, with a PTFE binder and with a Nafion binder.	16
Figure 2.7	Discharge capacity versus cycle results from two experiments for a (a) PTFE-treated cell and (b) Nafion-treated cell. Lines between discrete data points are included for ease of interpretation. The average of the two data sets (yellow curve) demonstrates nearly identical capacities for the two binders. The repeatability of the experiments must be improved, in order to make definitive conclusions about the impact of varying binder types.	17
Figure 2.8	Nyquist plots for cells (a) without binder, (b) containing PTFE and (c) containing Nafion. The four curves in each subplot represent the cell before cycling, after 1 cycle, after 2 cycles, and after 10 cycles.	18
Figure 2.9	Equivalent circuit for EIS analysis	19
Figure 2.10	Alternate equivalent circuit under consideration.	20

Figure 2.11	EIS fit comparison. Symbols: data, Solid lines: fits. The line labeled “Best fit” (yellow curve) is for the circuit containing 2 RC elements. “Alternate fit” (orange curve) is for the circuit containing 1 RC element.	21
Figure 2.12	SEM images of binder coatings on carbon paper before battery cycling at x500 magnification for the following cases: (a) carbon paper (AvCarb MGL190), (b) commercially coated PTFE on carbon paper (Toray 030), (c) PTFE coated, (d) Nafion coated.	24
Figure 2.13	SEM images of binder coatings on carbon paper before battery cycling at x2000 magnification for the following cases: (a) commercially coated PTFE on carbon paper (Toray 030), (b) PTFE coated, (c) Nafion coated.	25
Figure 3.1	Theoretical model domain.	29
Figure 3.2	Li_2O_2 formation.	30
Figure 3.3	The double layer is the build-up of negative and positive charge at the interface of two phases.	32
Figure 3.4	Current and molar flux within the GDL, with boundary conditions at the air and separator interfaces.	36
Figure 3.5	Image used to determine the volume fraction of binder in a PTFE electrode.	38
Figure 3.6	Experimental data and model fit of discharge capacity versus cycle for (a) PTFE-treated cell and (b) Nafion-treated cell.	39
Figure 3.7	Available carbon surface area versus cathode depth.	39
Figure 3.8	Electrolyte volume fraction versus cathode depth.	40
Figure 3.9	Li_2O_2 volume fraction versus cathode depth.	40
Figure 3.10	O_2 concentration versus cathode depth	41
Figure 3.11	Li^+ concentration versus cathode depth	42
Table 2.1	EIS inputs/settings	13
Table 2.2	Fitted circuit elements for cells without binder, with PTFE and with Nafion.	22

LIST OF ABBREVIATIONS

Electrochemical Impedance Spectroscopy	EIS
Field Emission Scanning Electron Microscope	FESEM
Gas Diffusion Layer	GDL
Energy Dispersive X-ray Spectroscopy	EDS

ACKNOWLEDGMENTS

This thesis is the result of support and encouragement of many people and organizations. Thank you to the Department of Energy for their funding of this research project. Thank you also to the Mechanical Engineering Department for their excellent teaching and research faculty. I am a better engineer for taking classes from and researching with you. Thank you especially to my committee members, Dr. Jason Porter and Dr. Greg Jackson.

A huge “thank you!” goes to my advisor, Dr. Steven DeCaluwe and the CORES research group for being the best group of people to work with. Dr. DeCaluwe, thank you for being approachable and supportive. Thank you for pushing your students to not only become better researchers, but better people, too. To my fellow CORES group members, thank you for your kindness. Your friendship, computer-debugging help and short lessons on the whiteboard have not gone unnoticed. I will miss working with you.

To my family, thank you for the frequent phone calls and greeting cards wishing me well. I feel so fortunate to have you.

To Joe, I can’t quite put into words what your encouragement has meant to me, but know that this project would not have been completed without you, thank you.

To my strong, intelligent and kind sister.

CHAPTER 1

INTRODUCTION

1.1 Introduction

Li-O₂ batteries have been a significant research topic for addressing electric vehicle (EV) performance improvements. Li-O₂ batteries have a theoretical energy density of up to 3500 Wh/kg_{battery} [1] – a 2-3x improvement in density over current rechargeable battery technologies, such as Li-ion. Batteries with higher energy densities means electric vehicles with longer driving ranges, making EVs more attractive to a larger demographic. Experimental data from a study conducted on some 20 electric vehicles in 2018 showed a linear trend when comparing the driving range of an EV to its battery energy density (Wh/kg_{vehicle}). The Tesla Model 3 was among the highest, with a range of 310 miles and energy density of 410 kWh/kg_{vehicle} [2]. With the assumption that a vehicle equipped with a Li-ion battery will have similar mechanisms for battery energy transfer through the vehicle’s drive-train, a Li-O₂ battery has the potential to drive close to 1000 miles on a single charge.

Distance between charging stations is a limiting factor in EV viability. Many areas of the country have very few, if any, EV charging stations. This makes it difficult for EVs to become commonplace in non-urban areas when compared with an internal combustion engine that can travel 350+ miles on one tank with widely available fuel resources. Li-O₂ batteries can help with this issue and as a result could potentially reduce the amount of carbon emissions emitted by automobiles as the conversion to EV’s occurs more readily. Before Li-O₂ batteries can become commercially available, however, there are several issues to be addressed. As such, let us first look at how a Li-O₂ battery operates.

The typical Li-O₂ battery configuration is shown schematically in Figure 1.1. While fundamental research into new battery materials and designs are ongoing, Li-O₂ batteries are typically composed of a pure lithium metal anode, glass fiber electrolyte separator, and

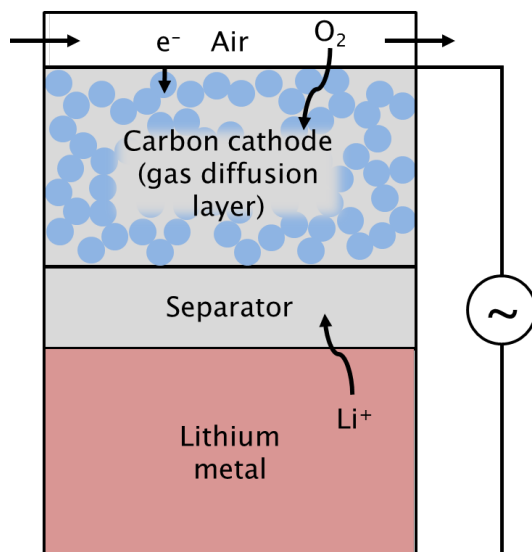
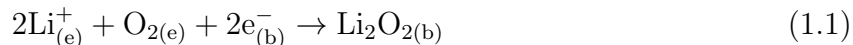


Figure 1.1: Schematic of Li-O₂ battery operation.

porous carbon-based gas diffusion layer (GDL) cathode. Electrolyte saturates both the GDL and separator. The carbon GDL interfaces with flowing air, and the components of the air (namely O₂) filter through the porous GDL structure as dissolved species in the electrolyte. During discharge, electrons flow through the carbon structure and Li⁺ ions move through the electrolyte, across the separator and into the cathode GDL. Two electrons, two Li⁺ ions, and an O₂ molecule meet at the interface between the carbon and electrolyte and react to form bulk lithium peroxide (Li₂O₂) according to the global reaction given below by Equation 1.1.



The reaction is controlled by how easily the electrons, Li⁺ ions, and O₂ molecules can reach each other. When the three reactants can no longer reach a common interface, the battery ceases its discharge. Surface area, therefore, becomes crucial for Li-O₂ battery performance.

The focus of this research is to gain a preliminary understanding of how certain aspects of a functional Li-O₂ battery affect its performance. Experiments conducted within this work give a look into physical battery behavior, as well as influence current theoretical modeling

techniques to further improve the understanding of this promising technology.

1.2 Li-O₂ Research and Development

Significant research has been done to improve the Li-O₂ electrolyte to better incorporate three desirable traits: the electrolyte should be (1) inert to nucleophilic attack on charge and discharge, (2) stable to metallic lithium, and (3) able to solvate lithium salts [3]. The most promising, as of 2015, was a mixture of dimethylacetamide (DMA) and dimethylformamide (DMF) with lithium bis(trifluoromethanesulfonyl)imide (LiTFSI) salt. Though stable, this combination reacts to form Li-X salts (X = formate, acetate and carbonate) which precipitate on the cathode leading to increased impedance and high cell polarization upon charging [3]. A study by Peng et al. presents a possible solution. Dimethyl sulfoxide (DMSO) electrolyte with nanoporous gold foil as the cathode results in products that do not passivate the cathode as severely as carbonates, and the electrolyte has a higher reactivity with lithium metal [4]. Thotiyl et al. proposed using tetraglyme (TEGDME) with a TiC cathode, finding good stability in regard to lithium, and a good electrochemical potential window [5]. However, the electrolyte, in this case, is susceptible to attack by a radical and form carbonates [3].

Additional work has been done to improve the cathode. Factors such as microstructure and electrode thickness impact O₂ diffusion to surface sites where the Li₂O₂ formation occurs. Additionally, electrode composition can influence the performance of Li-O₂ batteries [6]. Carbon has been the popular choice for the cathode material due to its lightweight properties, electronic conductivity, thermo-chemical stability, and low cost. The most desirable form of carbon is a carbon black powder – the powder increases battery capacity as the particles have a larger available surface area than a fibrous carbon paper. There are several different carbon powders used in studies: Super-P, Ketjan Black, Vulcan Carbon Powder, Black Pearls. Meini et al. compared first discharge capacity between cells with seven different carbon blacks, each having a unique surface area and porosity. The first discharge capacity is proportional to the externally accessible surface area of the carbon within the GDL. Additionally, they found that cells with TEGDME based electrolytes have 4x the initial

discharge capacity when compared with DME and DEGME [6]. Further research on the cathode involves transport of molecules and ions within the carbon. Collaboration between several institutions in Germany investigated the impact of micro- and meso-pores within the cathode on the discharge of a Li-O₂ battery. The pore structure had a significant influence on the transport and charge-transfer within the electrode. The more meso-pores within the material, the higher the specific surface area and therefore the higher the capacity. [7]. Work by Ottakam et al. questions carbon as a suitable cathode material. The formation of Li₂CO₃ from the dominant side-reactions involving the carbon cathode material and decomposition of the electrolyte occurs at a higher rate than Li₂CO₃ decomposition within the cathode. This leads to a build-up of Li₂CO₃, resulting in rapid polarization upon charging, electrode passivation and capacity fading upon cycling [8].

1.3 Current Challenges

There are four primary issues preventing Li-O₂ batteries from reaching their theoretical performance. The first deals with the battery's energy efficiency. There are significant losses incurred during battery cycling. The voltages produced by the battery during charging are much higher than during discharge. Therefore, even if the Coulombic efficiency is 100%, the energy put into the battery during charging is not fully recovered.

The ability to charge a battery quickly is very important for EV viability. Current Li-O₂ battery technology does not provide sufficiently high rate capabilities. This is due to two things. The first is Li₂O₂ resistivity. The electronic resistance of deposited Li₂O₂ increases as more is formed and the film thickens. This prevents further reduction of O₂ at the interface between the Li₂O₂ and electrolyte [6]. Additionally, research has found that Li₂O₂ forms near the separator at high charge rates, limiting transport of additional Li⁺ ions further into the cathode and the loss of available surface area resulting in a loss of capacity [9].

The third issue is due to how Li₂O₂ is formed and stored. The Li₂O₂ forms inconsistently – sometimes as a film and other times as a particle. The method by which the Li₂O₂ is stored affects how the reaction is run in reverse upon charging. Additionally, issues

with cyclability and material degradation reduce battery performance. The global reaction given above excludes some key intermediate reactions that take place within an active Li-O₂ battery. The products of some of these intermediate reactions attack certain components of the battery, such as the electrolyte, thus impacting the battery's cyclability [5].

The previous two issues discussed are enhanced by the binder. A binder is a polymer located within the GDL that has two main purposes: (1) bind the carbon particles together, and (2) ensure adhesion of the carbon particles to the current collector. The binder is especially important in GDLs in which carbon particles are used versus carbon fibers. Unlike the fibers, particles require a binder to maintain a porous shape for O₂ and Li⁺ transport. Particles provide more surface area than the fibers can and are therefore the standard for most Li-O₂ batteries. PvDF was the first binder to be used within Li-O₂ batteries as it is traditionally used in Li-ion batteries. Research found PvDF to be unstable under conditions in a Li-O₂ battery. Experiments and theory suggest that PTFE is more stable and is therefore the most commonly used today. Though PTFE has worked well in many Li-O₂ batteries, there is room for improvement. The most obvious concern is PTFE's lack of ionic conductivity. The binder contributes to additional material within the GDL that limits transport of ions and reduces available surface area. An ionically conductive polymer to replace PTFE would move Li-O₂ batteries toward their theoretical limit by promoting ion transport.

Studies by Amanchukwu, et al. [10], and Nasybulin, et al. [11] provide a short list of polymer binders stable against attack by Li₂O₂. Only Nafion has sufficient Li⁺ conductivity among those listed in the studies. Lithiated Nafion has therefore gained interest as a binder in Li-O₂ batteries. Due to its chemical and structural similarity to PTFE, it stands to reason that Nafion would share PTFE's stability. Several studies have investigated the effects of Nafion in Li-O₂ cells, post-cycling. For instance, Cheng et al. found improvements in both the cathode structure and electrochemical properties with the addition of a Nafion binder when compared with Kynar using TEM imaging and XRD [12]. However, no studies have yet examined Nafion's function in an active Li-O₂ cell. There are questions regarding Nafion's

long-term stability within a Li-O₂ battery. Additional questions remain regarding how much more Li₂O₂ can be generated and where it is stored. Depending on transport properties and reaction kinetics, the Li₂O₂ could be stored in any or all of three places: (1) traditionally, at the interface between electrolyte and carbon, (2) at the interface between electrolyte and Nafion, and/or (3) within the binder at the interface between carbon and Nafion (Figure 1.2). Answering these questions and understanding the fundamental physics will not only impact additional experiments and future improvements to Li-O₂ batteries, but theoretical models as well.

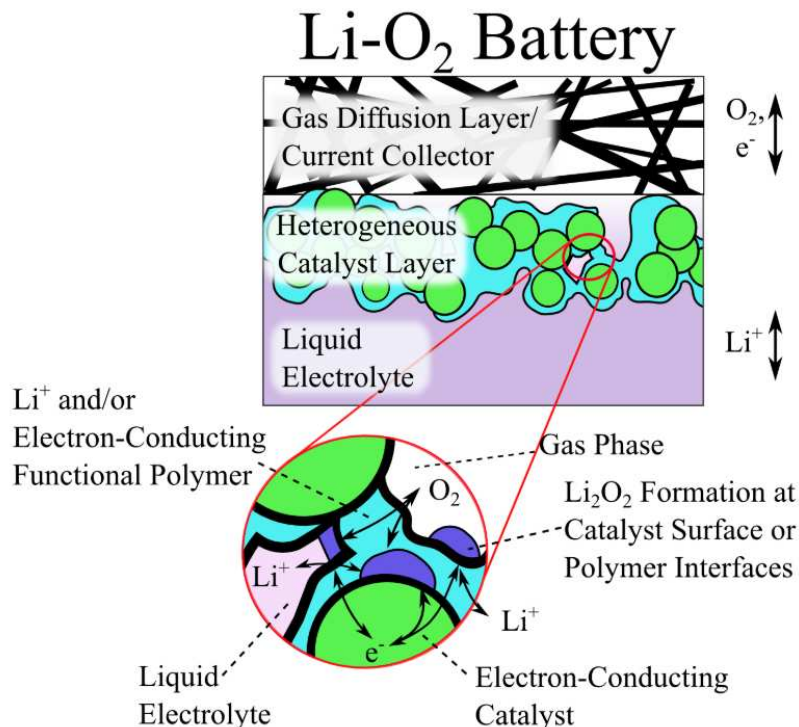


Figure 1.2: Visualization of the possible locations for Li₂O₂ formation within the battery's GDL. This figure was taken from the Department of Energy funding proposal [13].

1.4 Thesis Overview

Given the importance of the binder, this work seeks to understand the role of a Nafion binder in a Li-O₂ battery cathode using electrochemical experiments and a 1-D theoretical model. With combined Li-O₂ battery experiments and simulations, this project will quantify

the impact of novel conductive binders on battery performance. The experimental results demonstrate the impact of binder loading and conductivity on battery performance. Battery charge and discharge data is collected for varying coating techniques of two different polymers: a non-conductive PTFE binder and a conductive lithiated Nafion binder. Validation of a one-dimensional Li-O₂ battery model against this battery data provides an avenue for quantifying the impact of conductive and non-conductive binders on battery performance. This validated model, in turn, will help to develop conductive polymer binders and battery microstructures for efficient and durable Li-O₂ batteries.

Part of a larger project funded by the Department of Energy (DOE) intended to study active polymer interfaces, this project tackles only one facet of the overall goal. The goal for the Li-O₂ battery portion as stated in the DOE project proposal is as follows:

1. How does polymer dispersion and structure affect its properties in an operational Li-O₂ cathode?
2. What are the dominant oxidation and reduction pathways at Nafion interfaces in Li-O₂ batteries?

Of course, answering these questions requires a significant amount of time, infeasible for the length of an MS program. The contribution of this thesis is therefore focused on the following questions:

1. How does the battery performance change as a function of binder loading?
2. How do experimental results influence the model approach?

The format of this thesis is as follows: Chapter 2 will discuss experimental methods and the results from the various experiments. Chapter 3 gives information regarding the framework and results of the 1-D theoretical model of the Li-O₂ battery. Chapter 5 summarizes the work, provides conclusions of the entire thesis and gives next steps for the project.

CHAPTER 2

EXPERIMENTAL CHARACTERIZATION OF LI-O₂ BATTERIES

2.1 Introduction

A major goal of this thesis is to provide insights to the design of Li-O₂ cathode design, via numerical simulation tools. However, numerical simulations to predict the impact of conductive and non-conductive binders require a number of input parameters that relate to the microstructure, properties and mechanistic differences of the binder. These characteristics are not well understood, which prevents the use of simulations to guide material development and cathode/GDL design. Therefore, the experiments conducted in this project have two purposes: (1) to gain a better understanding of how a Nafion binder affects a Li-O₂ battery cell's performance, and (2) to learn behavior (i.e. transport) of the cell components with the addition of polymer binders (Teflon and Nafion) to improve the accuracy of current Li-O₂ theoretical modeling. This chapter describes the assembly, experimental procedures and characterization of Li-O₂ battery cells. Basic Li-O₂ cells were tested first, using a GDL without a binder (AvCarb MGL190) to get baseline data for comparison with future tests. These tests were repeated with PTFE and Nafion binders added to the carbon paper. The cells were compared using electrochemical tests such as charge/discharge curves, capacity vs. cycle number and galvanostatic electrochemical impedance spectroscopy. Other characterization methods include FESEM imaging of cathodes to gain qualitative information about binder dispersion.

2.2 Methods

The following describes the steps taken to prepare the battery materials and assemble the batteries for testing. In all steps, great care was taken to remove moisture from all battery component chemicals and materials.

2.2.1 Electrolyte preparation

Great care is required, during electrolyte preparation, to remove moisture from all component chemicals, which will degrade battery performance. Tetraethylene glycol dimethyl ether (tetraglyme) (TEGDME, Sigma-Aldrich) was dried over 4 Å molecular sieves for 2 hours at 40°C in an Argon filled glovebox (LC Technology Solutions) and further dried overnight in a vacuum furnace at 80°C. Bis(trifluoromethane)sulfonimide lithium salt(LiTFSI) powder (Sigma-Aldrich) was dried overnight in a vacuum furnace at 80°C. After drying, both the TEGDME and LiTFSI were returned to the glovebox. The LiTFSI was added to a glass jar of TEGDME and stirred until completely dissolved. The 1 M LiTFSI in TEGDME solution was stored in the Argon filled glovebox.

2.2.2 Cathode preparation

Three different types of cathodes were used for the aforementioned experiments. As a control, batteries were assembled with binder-free carbon paper. These results were compared with those for carbon-paper cathodes with two different binders: non-conductive PTFE and ion-conducting Nafion. Note that, although the typical function of the binder is to provide contact between cathode particles and the current collector as a means to increase available surface area, no particles are used in these experiments. As such, the carbon paper serves as a model system, to characterize the impact of binder on the Li-O₂ battery performance. The goal of the model system, in this instance, is to isolate the impact of the binder, without any confounding artifacts from the microstructure of carbon black particle agglomeration, for example.

Carbon paper processing: Prior to electrochemical testing, carbon paper (AvCarb MGL190 FuelCell Store) was dried under vacuum at 200°C overnight and transferred to the glovebox, avoiding further contact with ambient air. Binder-free electrodes used for FESEM imaging were used as they arrived from the manufacturer.

Binder addition: Carbon paper disks cut to 18 mm diameter were soaked in binder dispersion for 4 hours in a beaker. The conductive Nafion binder dispersion was 10 wt% LITHion (Nafion Store) in isopropanol, and the non-conductive binder dispersion was 60 wt% PTFE (Sigma Aldrich) in H₂O, which was further diluted with isopropanol, to match the LITHion dispersion at 10 wt% PTFE. Excess dispersion was drained after soaking, and the disks were left in the fume hood for evaporation of the solvent (about 30 minutes). Cathode disks were then dried in a vacuum furnace at 95°C for 6 hours. Treated disks were transferred to the argon-filled glovebox to avoid contamination.

2.2.3 Cell preparation and assembly

Electrochemical measurements were carried out using a commercially available 3-electrode ECC-DEMS cell (EL-cell GmbH, Germany) equipped with inlet and outlet ports for gas purging. A cross-section view of the cell with labels for key components can be seen in Figure 2.1. Lithium disks punched using an 18 mm hole-punch from EL-cell acted as the counter and reference electrode. Carbon paper was hole-punched to size and acted as the cathode/GDL, and a Whatman glass fiber disk was the separator.

The cell was assembled in an argon-filled glovebox. The PEEK sleeve was first inserted in the main body of the cell and locked in place with the reference pin. The carbon electrode was then placed in the bottom of the sleeve, followed by the separator and 500 μ L of 1 M LiTFSI in TEGDME electrolyte. Lithium metal was placed on top of the saturated separator, and the cell was sealed. The gas inlet and outlet were sealed using ball valves, and the cell was left to rest in the glovebox for 6 hours to allow for complete diffusion of the electrolyte within the carbon electrode and separator. The battery was then taken out of the glovebox to a fume hood with mass flow controllers to control the flow of dry O₂. The cell was purged with UHP O₂ at 3 mL/min for 60 minutes while open circuit voltage (OCV) was recorded using a potentiostat (Gamry Reference 600). Figure 2.2 gives a reference for battery electrode and gas port set-up.

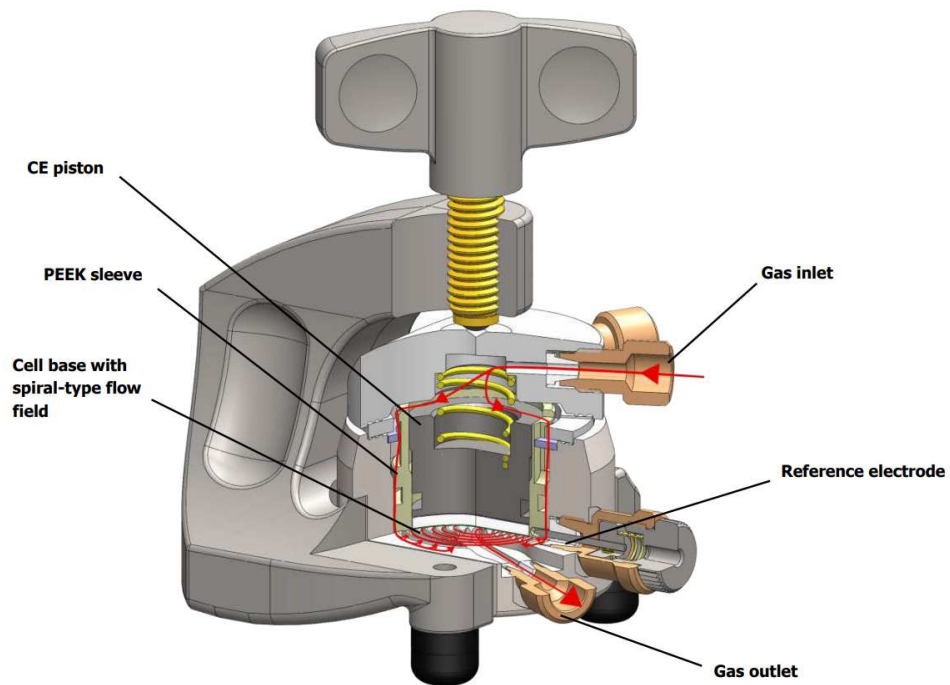


Figure 2.1: Cross-sectional view of the ECC-DEMS cell [14].

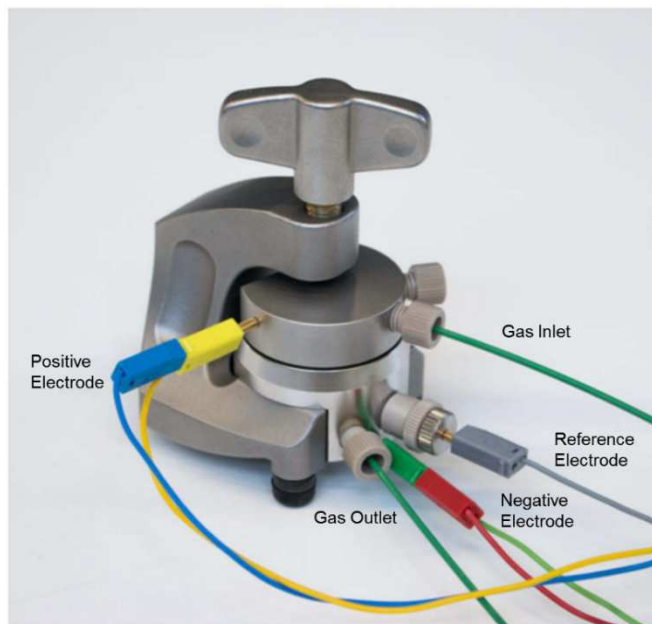


Figure 2.2: Electrode and gas port connections for battery cell based on EL-cell ECC-DEMS user manual [14].

2.2.4 Cell disassembly and cleaning

After testing, the cell was returned to the glovebox and disassembled. Cell parts including the lid and spring were cleaned in DI water in an ultrasonic bath for 1 hour. They were then allowed to air dry before being dried in a vacuum furnace at 80°C overnight. The cleaned cell parts were placed in the glovebox for storage to avoid unwanted contamination.

Step-by-step instructions for cell assembly and disassembly can be found in Appendix A.

2.3 Experimental Methods

Three methods were used to evaluate the performance/state of the cell: discharge capacity degradation, galvanostatic electrochemical impedance spectroscopy and field emission scanning electron microscope imaging. Details of each method are described below.

2.3.1 Discharge capacity vs. cycle number

Cells were discharged (lithium to the cathode) and charged (lithium to the anode) at a constant current of 1 mA between -2 V and -4.5 V (vs. Li/Li⁺). Each cell tested was cycled 10 times to monitor the degradation of the battery capacity over the course of the battery cycling. While batteries should ultimately be capable of thousands of cycles, 10 cycles were used here as a snapshot of the battery's initial performance. Comparing the capacity versus cycle number between the different cells gives an indication of overall battery performance and detrimental interactions occurring within the battery with the introduction of the different binders. The discharge capacity was calculated as:

$$cap = \frac{tI}{m}$$

where t is the time of discharge in seconds, I is the applied current in A, and m is the mass of carbon in the GDL in grams. The mass of carbon was calculated using the volume, density and porosity of the carbon paper, as supplied by the manufacturer.

2.3.2 Electrochemical impedance spectroscopy

Electrochemical impedance spectroscopy (EIS) is used to evaluate the dynamic response of an electrochemical device. Galvanostatic EIS is measured by applying an AC perturbation to a steady state DC current, and measuring the cell voltage. The impedance response is measured for a range of frequencies, which provides insight to the range of limiting processes occurring in the device. The impedance is expressed in terms of a magnitude Z_0 and a phase shift ϕ . The Nyquist plot compares the negative of the imaginary part of the impedance Z_{imag} versus the real part Z_{real} . From the Nyquist plot you can gain information regarding the resistance and capacitance of different processes occurring within the cell, as well as information about transport through the cell.

The EIS tests were run using the Gamry potentiostat with the settings in Table 2.1.

Table 2.1: EIS inputs/settings

Initial frequency (Hz)	1e5
Final frequency (Hz)	0.1
Points/decade	1.0
DC current (A)	0.0
AC current (A rms)	1.0e-4
Estimated Z (Ω)	1.0e2

2.3.3 Field emission scanning electron microscopy

High-Resolution field emission scanning electron microscopy (FESEM) (JEOL 7000 FESEM) imaging was used to qualitatively compare the electrodes. Secondary Electron FESEM images was used to understand how the binder was incorporated into the GDL and which binder electrode preparation method produced the most consistent GDL structure. All samples imaged are cross-sections of the carbon electrodes to provide bulk analysis rather than analysis of surface effects.

2.4 Experimental Results

2.4.1 Capacity vs. cycle number

The charge-discharge curves for 10 cycles of each cell are given in Figure 2.3 (no binder), Figure 2.4 (PTFE binder), and Figure 2.5 (Nafion binder). While the discharge curves (negative-going potential) show little variation as a function of cycle number, the charge curves (positive-going potential) show decreasing charge with increasing cycle number. The decrease in charging capacity is greatest in the non-binder cell (Figure 2.5), and smallest in the cell containing PTFE (Figure 2.4). In general, the results are typified by large over/underpotentials—the charge and discharge occur at voltages more than 0.5 V above and below, respectively, the predicted equilibrium potential. The large potential drops are likely a result of the low-surface area carbon paper cathode (an idea explored below in Chapter 3), and result in termination of the charge and discharge processes due to hitting the potential limits. Complete charge or discharge would be observed as a sharp change in the slope of the curve toward negative or positive infinity, respectively. The absence of any such limiting capacity indicates that the charge and discharge processes all terminate before the cathode has been completely charged or discharged, but are rather terminated to prevent the battery from reaching potentials at which deleterious side reactions become thermodynamically favorable.

Figure 2.6 summarizes the total discharge capacity as a function of cycle number for all three electrode types. Over the course of 10 cycles at 1 mA, the battery treated with PTFE dropped from a capacity of 0.026 mAh/g_{carbon} to 0.010 mAh/g_{carbon}. In comparison, the capacity of the battery treated with Nafion went from 0.040 mAh/g_{carbon} to 0.020 mAh/g_{carbon}. The cell without binder dropped from a maximum capacity of 0.036 mAh/g_{carbon} to 0.032 mAh/g_{carbon}. As predicted, the no-binder cathode gives the largest discharge capacity. Adding binder blocks pores and covers surfaces, but without the typical benefit, in this case, of increased surface area from carbon black or catalyst particles.

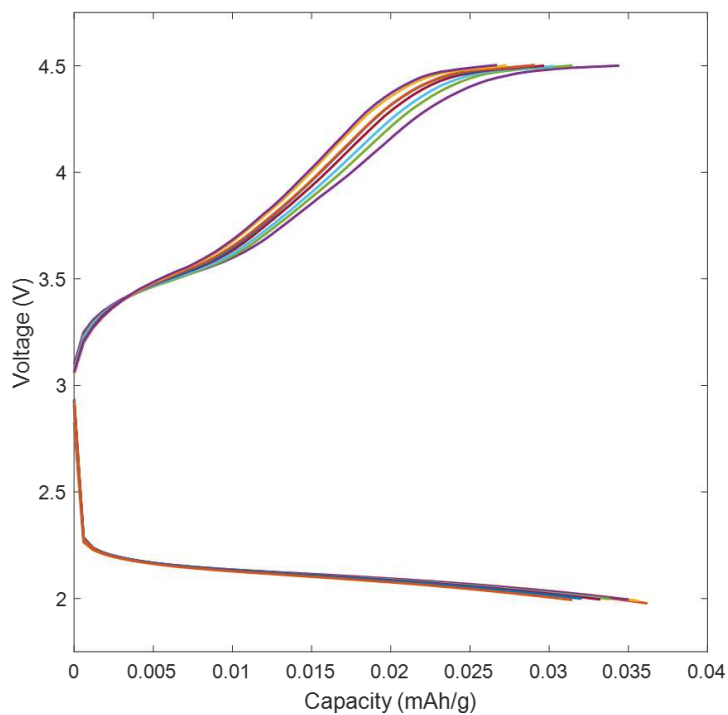


Figure 2.3: Charge-discharge curves for a Li-O₂ cathode with no binder. The cell was cycled at 1 mA between 2 and 4.5 V.

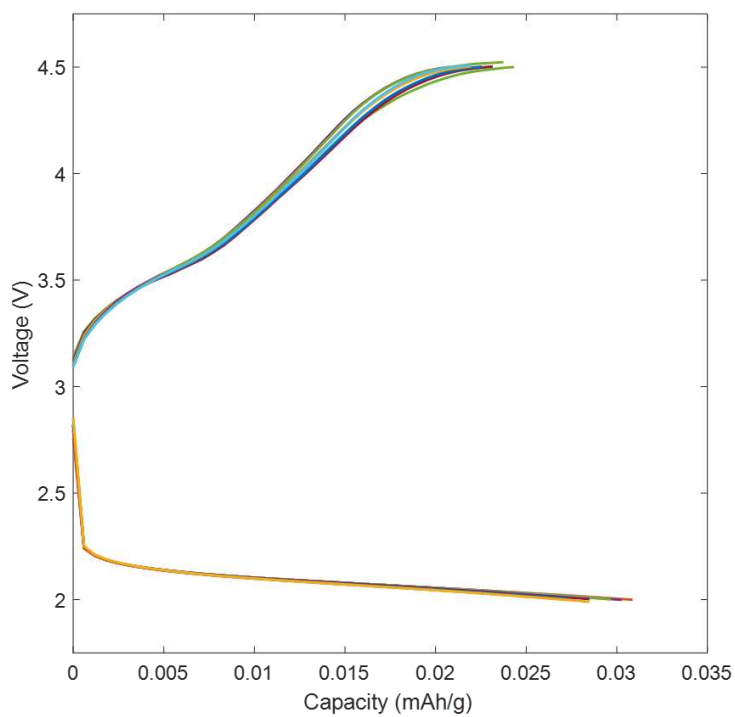


Figure 2.4: Charge-discharge curves for a Li-O₂ cathode with PTFE binder. The cell was cycled at 1 mA between 2 and 4.5 V.

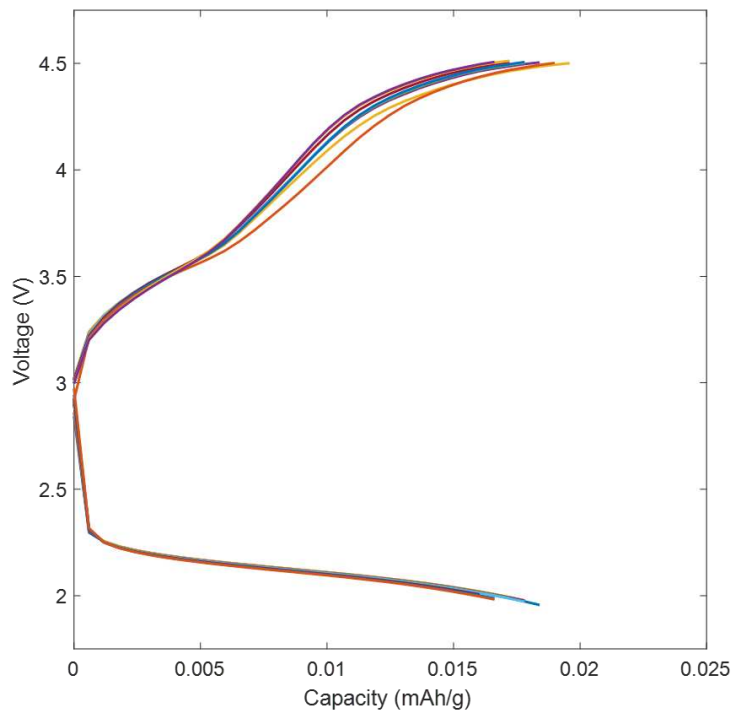


Figure 2.5: Charge-discharge curves for a Li-O₂ cathode with Nafion binder. The cell was cycled at 1 mA between 2 and 4.5 V.

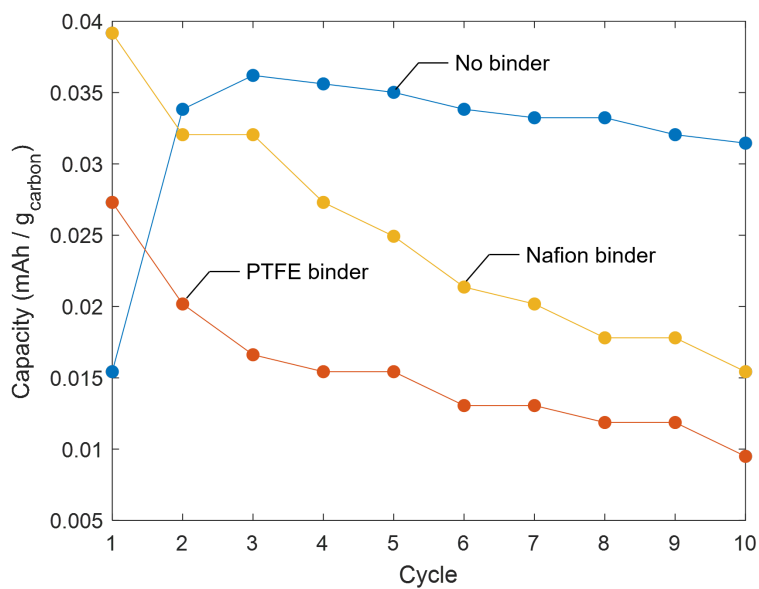


Figure 2.6: Discharge degradation of cells without a binder, with a PTFE binder and with a Nafion binder.

2.4.2 Repeatability

Two test the repeatability of the data, the experiments from Figure 2.3–Figure 2.6 were repeated on a new set of cathodes. Figure 2.7 shows the results of discharge capacity versus cycle number for the PTFE- and Nafion-treated electrodes. The Nafion cell has starkly different capacities in the first few cycles but the capacities converge to an almost identical point. The PTFE cell, on the other hand, keeps approximately the same capacity difference over the course of the cycling. In contrast to the first set of experiments, the PTFE-treated cell has higher discharge capacity than the Nafion-treated cathode, such that the average capacities are nearly identical for the two cells—the difference between the ‘Average’ data for the two binders is certainly much less than the sample-to-sample variation between the repeated experiments. The low repeatability therefore prevents from making any conclusive observations, at present, about the relative merits of the conductive Nafion binder.

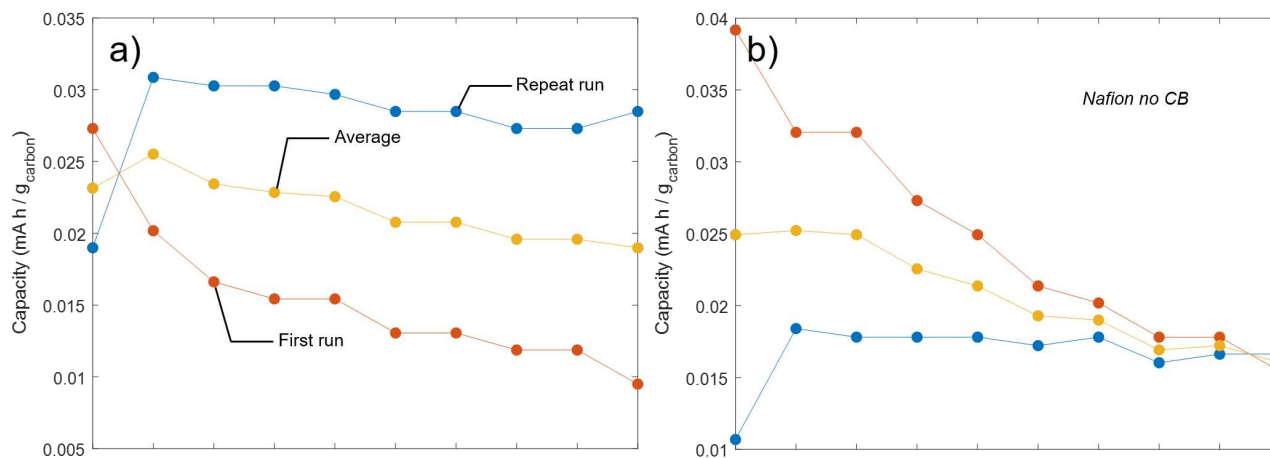


Figure 2.7: Discharge capacity versus cycle results from two experiments for a (a) PTFE-treated cell and (b) Nafion-treated cell. Lines between discrete data points are included for ease of interpretation. The average of the two data sets (yellow curve) demonstrates nearly identical capacities for the two binders. The repeatability of the experiments must be improved, in order to make definitive conclusions about the impact of varying binder types.

2.4.3 Electrochemical impedance spectroscopy

Figure 2.8 shows the progression of EIS curves for all three electrode types. Curves are shown before cycling, after 1 cycle, after 2 cycles and after 10 cycles. The impedance decreases with cycle number in all three cases. Additionally, the high frequency arc is smaller for the Nafion cell than the other two. These variations are minor, and additional analysis via equivalent circuit analysis is necessary.

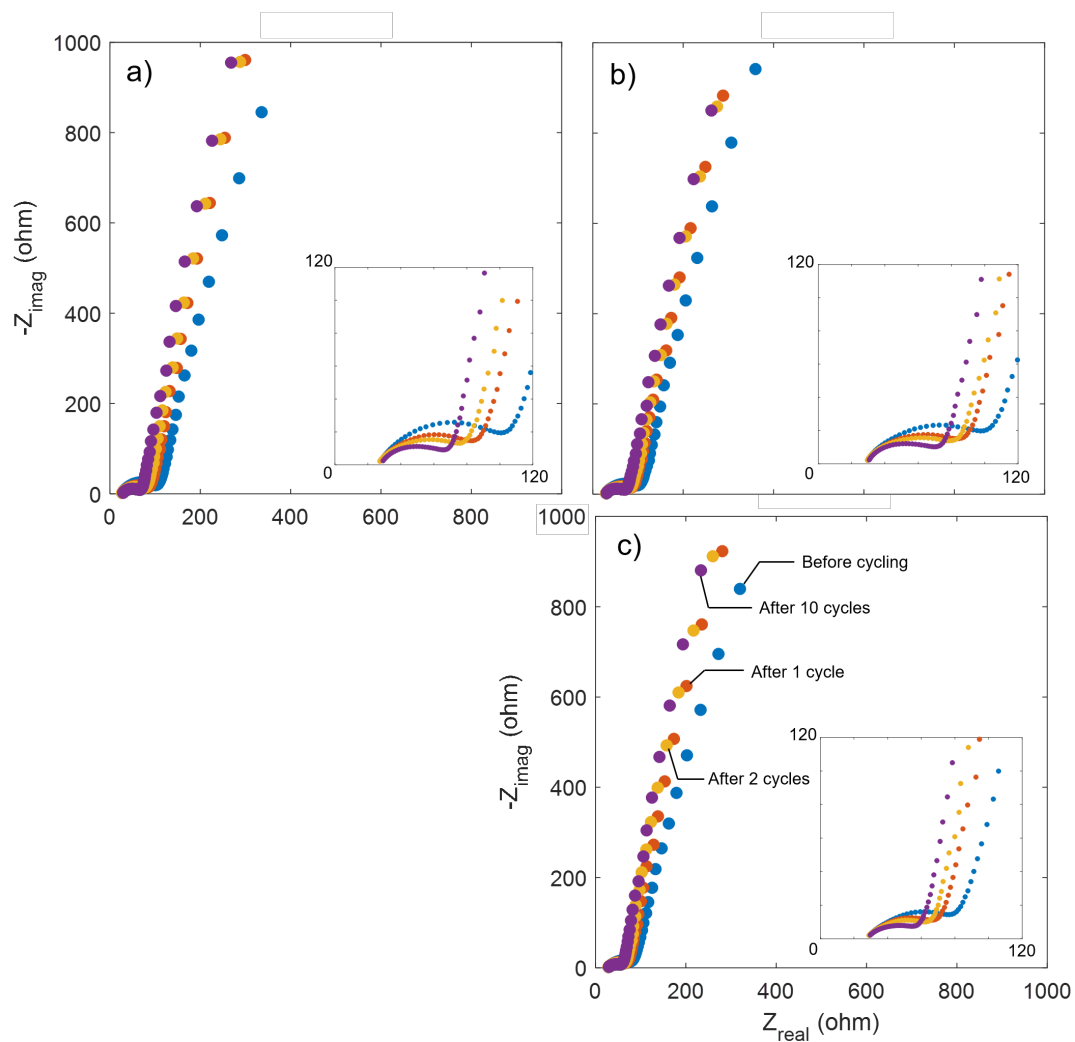


Figure 2.8: Nyquist plots for cells (a) without binder, (b) containing PTFE and (c) containing Nafion. The four curves in each subplot represent the cell before cycling, after 1 cycle, after 2 cycles, and after 10 cycles.

Equivalent circuit fits, as shown in Figure 2.9 and Figure 2.10 quantified the trends observed in the impedance data. Two possible equivalent circuits, with a varying number of elements, were considered. The first circuit considered is shown in Figure 2.9. The resistor on the left of the circuit labeled *Contact Resistance* encompasses contact resistances, and resistance due to mass transport through the separator and GDL. The two RC elements represent the electrochemical reactions taking place within the cell. The farthest left represents the reaction that forms Li_2O_2 in the cathode ($2\text{Li}^+ + \text{O}_2 + 2e^- \rightarrow \text{Li}_2\text{O}_2$), and the right element represents the reaction that changes lithium from its bulk phase in the anode to the electrolyte phase in the separator ($\text{Li}_{(b)} + e^- \rightarrow \text{Li}_{(e)}^+$). The Warburg element labeled *Transport* includes mass transport within the electrolyte. Finally, the capacitor on the right of the circuit represents the *Non-ideal Capacitance*. The capacitance of the battery is proportional to the battery's state of charge (SOC). In areas of the polarization curve where the voltage of the cell changes quickly as a function of the SOC, the capacitance will have a different value than in an area where the voltage is relatively constant as a function of the SOC.

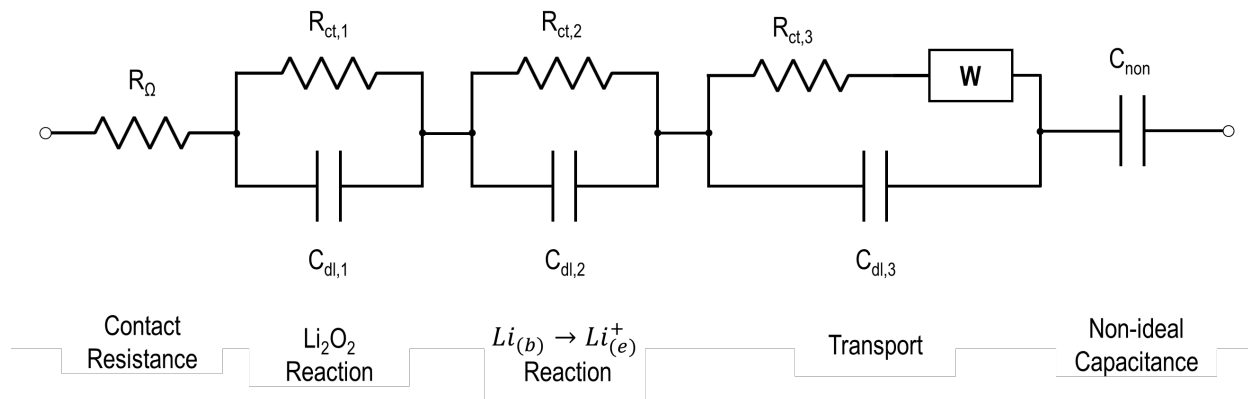


Figure 2.9: Equivalent circuit for EIS analysis

Fits from this circuit were compared to those from a circuit with fewer elements, to verify that we were not ‘over-fitting’ the data. Adding more parameters to a fit should, in theory, always improve the fit, but one must evaluate whether or not the improvement was statistically meaningful. A Bayesian Information Criterion (BIC) fitting algorithm was used

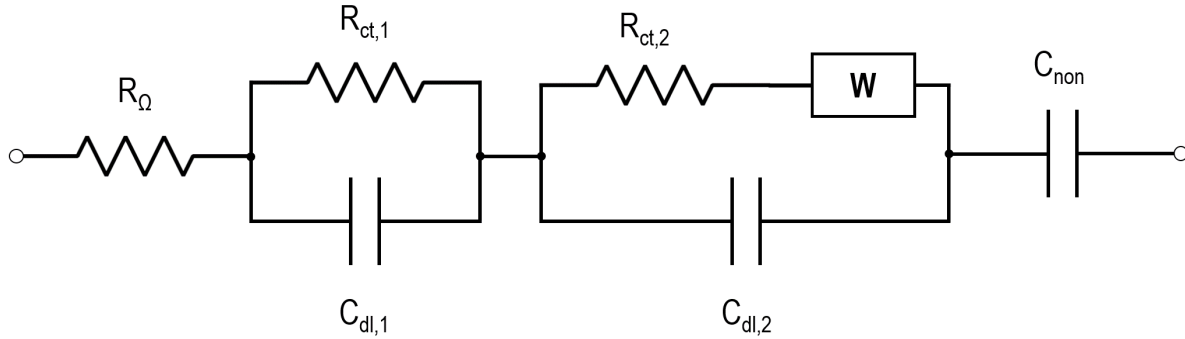


Figure 2.10: Alternate equivalent circuit under consideration.

to compare the two circuits while considering how many parameters are used. The BIC is essentially a log-likelihood goodness-of-fit function, penalized proportional to the number of parameters:

$$\text{BIC} = n \ln \frac{\text{RSS}}{n - 1} + k \ln n$$

where n represents the number of data points within the dataset and k is the number of parameters in the circuit under consideration. RSS is the residual sum of squares, given as

$$\sum \frac{(\text{fit} - \text{data})^2}{\sigma^2}$$

where σ^2 is the data's variance taken as 1% error in each data point given by the instrument manufacturer (*Gamry*). A lower BIC indicates a better fit of the data, and the fit is penalized for increasing k , the number of fitting parameters. For a given dataset, a BIC difference between circuits of at least 5 points shows a statistically meaningful difference between the two model fits, and the fit with the lower BIC is considered a better fit. Any difference lower than 5 shows the fits are not significantly different. The BIC was calculated for each equivalent circuit using data from some 15 datasets, and showed the equivalent circuit with two RC elements shown in Figure 2.9 fit the data better than Figure 2.10 without

extra R - C element. The best fit is also apparent from a plot of the two fits, as in Figure 2.11. Particularly at the high-frequency portion of the curve, the “Best fit” shows improvement over the “Alternate fit.” The addition of a second RC element therefore helps capture the higher frequency curve in a statistically meaningful way.

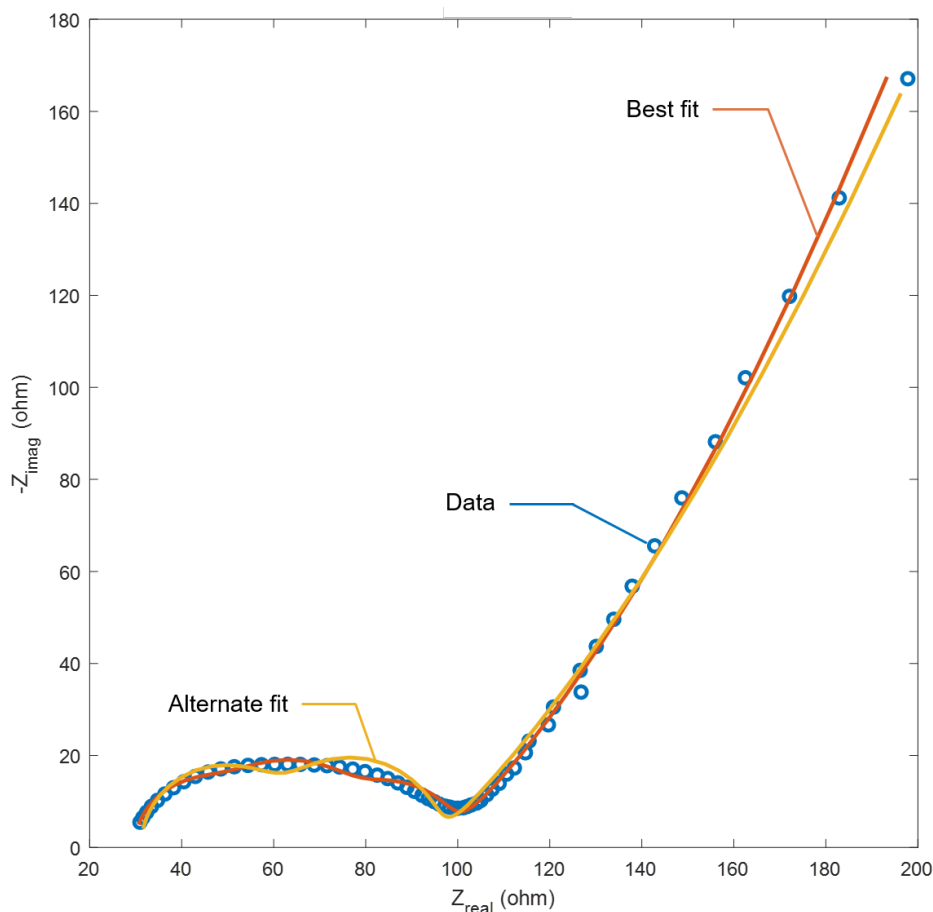


Figure 2.11: EIS fit comparison. Symbols: data, Solid lines: fits. The line labeled “Best fit” (yellow curve) is for the circuit containing 2 RC elements. “Alternate fit” (orange curve) is for the circuit containing 1 RC element.

Table 2.2 shows the fitted values for the different elements in the equivalent circuit for PTFE- and Nafion-treated cells, and cells without binder. The ohmic resistance R_{Ω} of the PTFE and Nafion cells are very similar, with Nafion having a slightly higher resistance. The non-binder ohmic resistance is lower than the other two by about 1.5Ω . The charge transfer resistance $R_{ct,1}$ is markedly different for the Nafion cell. The charge transfer resistance in

the PTFE and non-binder cells is over twice the resistance of the Nafion cell before cycling, and about 25% higher after 10 cycles. Nafion also has a higher double-layer capacitance $C_{dl,1}$ both before and after cycling. A different trend is observed for the second RC element: charge-transfer resistance $R_{ct,2}$ and double-layer capacitance $C_{dl,2}$. Prior to cycling, PTFE has the lowest resistance, followed closely by the non-binder cell, and the highest capacitance. After cycling, however, the non-binder cell has the highest resistance, followed by the PTFE cell, which has the highest capacitance.

The third charge transfer resistance $R_{ct,3}$ of the non-binder cell is higher than the PTFE and Nafion cell prior to cycling, but the PTFE cell has the highest resistance after cycling. The double-layer capacitance $C_{dl,3}$ is lowest for the PTFE cell in both cases. The Warburg element is highest for the Nafion cell in both cases, with the scale of the element increasing twofold after 10 cycles of the battery. Prior to cycling, the non-ideal capacitance C_{non} is highest in the non-binder cell. After cycling, however, C_{non} is highest in the Nafion cell.

Table 2.2: Fitted circuit elements for cells without binder, with PTFE and with Nafion.

	Before Cycling			After 10 Cycles		
	None	PTFE	Nafion	None	PTFE	Nafion
R_{Ω} (Ω)	27.5	29.1	29.2	29.2	30.4	29.1
$R_{ct,1}$ (Ω)	28.4	30.4	12.4	11.0	12.7	9.21
$C_{dl,1}$ (F)	1.26e-5	1.00e-5	3.10e-5	2.15e-5	1.69e-5	2.77e-5
$R_{ct,2}$ (Ω)	7.50	6.56	9.17	9.53	5.65	4.97
$C_{dl,2}$ (F)	1.28e-6	9.36e-3	6.92e-7	1.15e-6	1.16e-6	1.01e-6
$R_{ct,3}$ (Ω)	25.1	19.3	18.0	11.8	15.7	9.54
$C_{dl,3}$ (F)	2.99e-6	2.27e-6	4.62e-6	4.62e-6	2.17e-6	3.54e-6
W ($Ss^{1/2}$)	3.12e-3	2.84e-3	3.30e-3	5.70e-3	4.38e-3	6.72e-3
C_{non} (F)	1.00e-3	8.99e-4	9.73e-4	9.62e-4	9.12e-4	1.04e-3

2.4.4 FESEM imaging

FESEM was used to compare the binder coating between the two polymers as well as coating techniques from a high-level observational point of view. All samples imaged are cross-sections of the carbon electrodes to provide bulk analysis rather than analysis of surface effects. Figure 2.12 compares the different electrodes before cycling, but after binder addition (if applicable). Figure 2.12(a) shows a cross-section of the binder-free carbon paper (AvCarb MGL190). Overall, the carbon fibers are visibly free from contaminants or other species. The sharp edges that can be seen are assumed to be from brittle fracture of the carbon fibers from cross-sectioning. This figure becomes the control to which the remainder of the samples are compared.

To compare our in-house binder deposition to a commercial surrogate, commercially coated PTFE on carbon paper (Toray Paper 030) is shown in Figure 2.12(b). Apart from the PTFE coating and total thickness of the paper, the carbon microstructures of the Toray and carbon papers are manufactured to be identical (i.e. structure, porosity). The strands appear to be evenly coated relatively uniformly by PTFE within the pores near the bottom of the image. In comparison, our in-house PTFE coating in Figure 2.12(c) looks significantly different when compared to the commercially available Toray paper. In the in-house electrode (Figure 2.12(c)), the PTFE appears in clumps, rather than evenly coating the fibers, likely due to agglomeration from the process and poor interfacial bonding. Additionally, web-like strands are visible within the open spaces with small masses suspended on them.

The Nafion-coated electrode is shown in Figure 2.12(d). The Nafion is coated inconsistently along the vertical direction of the cross-section. Smooth, solid pieces of what is presumably Nafion appear at the bottom of the image, while sharp, thin pieces of Nafion can be seen near the top of the image.

Figure 2.13 compares the methods for coating the carbon fiber paper in binder, at a higher magnification (x2000). Toray paper, a PTFE-coated electrode, and a Nafion-coated electrode are considered. The Toray paper has a very uniform coating. Each strand is

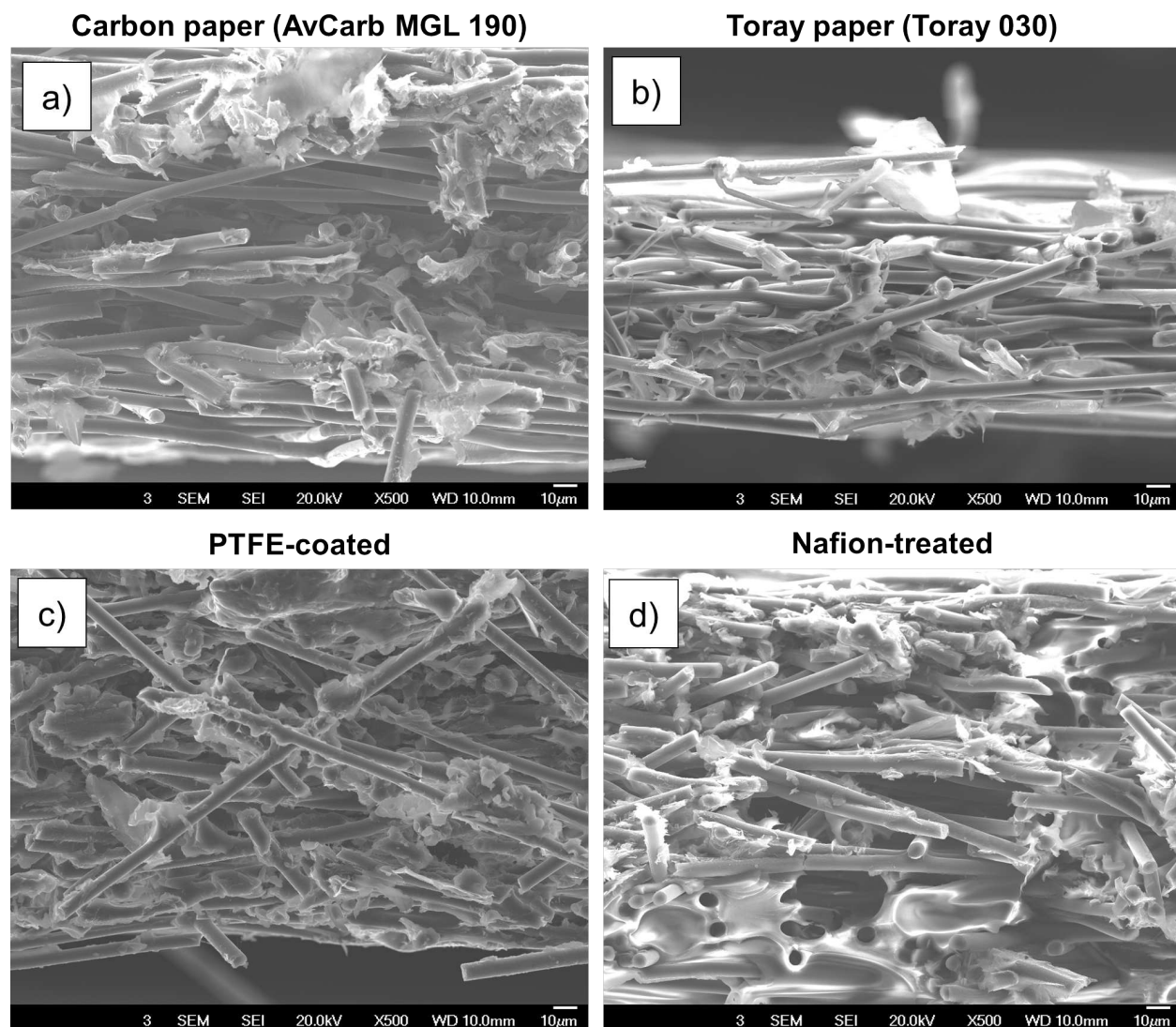


Figure 2.12: SEM images of binder coatings on carbon paper before battery cycling at x500 magnification for the following cases: (a) carbon paper (AvCarb MGL190), (b) commercially coated PTFE on carbon paper (Toray 030), (c) PTFE coated, (d) Nafion coated.

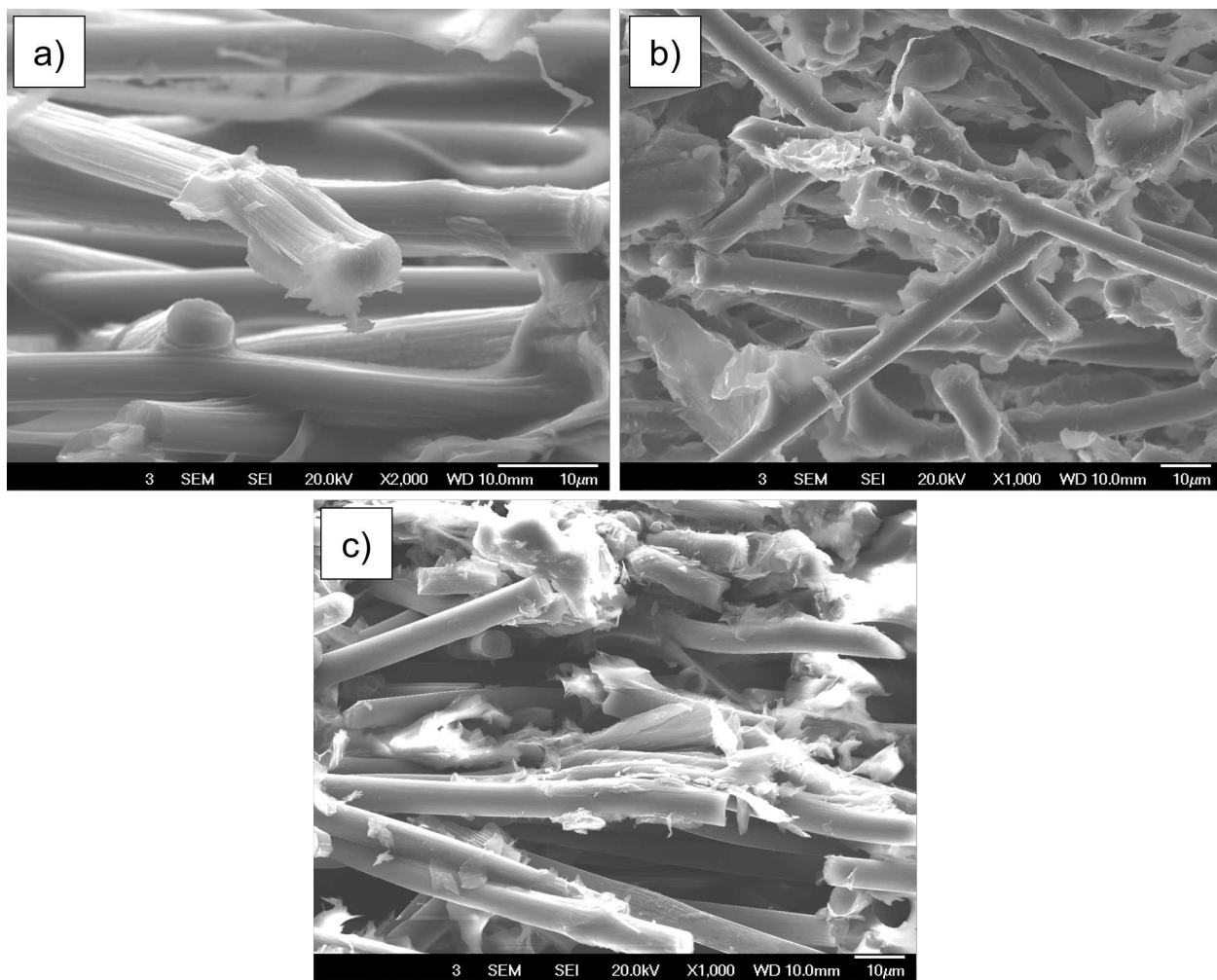


Figure 2.13: SEM images of binder coatings on carbon paper before battery cycling at x2000 magnification for the following cases: (a) commercially coated PTFE on carbon paper (Toray 030), (b) PTFE coated, (c) Nafion coated.

covered in the PTFE, and little of the pore space is affected. The in-house PTFE-coated electrode is less uniform, with the PTFE appearing in clumps on the fibers. This is to be expected, with unoptimized binder incorporation procedures (at least compared to industrially manufactured Toray paper). In the Nafion electrode, the Nafion is visible as flakes within the electrode, and does not appear well-adhered to the carbon fibers. In both in-house electrodes, the binder appears in bulk-like clumps, rather than films, which could have significant implications on transport and Li_2O_2 formation within the GDL, as well as on the sample-to-sample variations observed above in Figure 2.7.

2.5 Discussion

The overall capacity of all battery cells was significantly lower than both the theoretically calculated value ($810 \text{ mAh/g}_{\text{carbon}}$) and results from similar investigations [15–17]. This is expected, due to the use of the low-surface area carbon paper as our model system. Unfortunately, two aspects of the cell fabrication prevent definitive conclusions about the impact of binder type on Li-O₂ battery performance. First, the low surface area results in significant potential losses, even at very low currents, such that the charge and discharge processes are terminated by hitting thermodynamically-determined voltage limits, rather than by the complete charge and/or discharge of the battery. The charge/discharge capacities reported are therefore measures of the voltage drop as a function of cycle number, rather than a direct indicator of the cathode’s Li storage capacity. Second, repeated testing revealed significant sample-to-sample variations in battery performance, such that the relative performance of PTFE-coated vs. Nafion-coated cathodes varied, from test-to-test.

When comparing the fitted equivalent circuit parameters for the EIS data from the first round of experiments in Table 2.2, the resistances (ohmic and charge-transfer) in the Nafion-treated cell are all lower than the PTFE-treated with the exception of second charge-transfer resistance $R_{ct,2}$, where the resistance in the PTFE cell is lower by about 2.75Ω . These lower resistances could contribute to Nafion’s higher performance in terms of discharge capacity. The difference in R_Ω between the cells shows that the conductivity of the binder does not

have a significant effect on the cell's contact resistance.

Another trend that becomes apparent is the higher capacitances in the Nafion cells, with the exception of the second double-layer capacitance $C_{dl,2}$, where the PTFE cell has a higher capacitance by about 2.5×10^{-7} F.

The higher Warburg impedance in Nafion-treated cells could also explain the improved performance in Nafion cells in the first round of experiments. A higher Warburg impedance is an indication of a higher diffusion coefficient. The conductivity of the Nafion binder could be responsible for this – the Nafion could possibly be promoting diffusion through the GDL and therefore increasing the discharge capacity of the battery.

Though the coating procedures for the Nafion and PTFE electrodes are identical, the PTFE electrode has a much more consistent coating than Nafion, as revealed by SEM imaging. There is a possibility that the inconsistency lies in the structural difference between PTFE and Nafion, namely the existence of a side-chain off Nafion's PTFE backbone. Whereas the PTFE molecule is largely inert, the ionic Nafion side-chain can lead to inter-molecule interactions and agglomeration, leading to the solid structure in the bottom of the image. Settling of the Nafion dispersion could also play a factor. Though impossible to identify which side of the electrode was facing down while the electrode was drying, this could have played a role in the inconsistent Nafion coating. The side facing down could have accumulated more Nafion as the solvent evaporated.

There are obvious differences between the different electrode fabrication techniques. These differences not only play a role in the electrochemical performance, but also impact how the binder is developed in theoretical models. Though the optimization of binders and dispersions is necessary for preferred operation, the refinement of the electrode fabrication process is beyond the scope of this project. Finally, it is worth noting that much of this FESEM analysis is speculative, as the images do not provide much quantitative information, such as material composition. The use of energy dispersive spectroscopy (EDS) could confirm and add to this discussion.

2.6 Conclusions

The results from the Li-O₂ cell experiments were largely inconclusive. The first round of testing showed an improvement in discharge capacity with the addition of a Nafion binder. However, the repeated experiments showed the opposite results. EIS taken with the first round of testing gave some indication as to why the Nafion cell had higher capacity - it had lower resistances and higher Warburg impedances, indicating better mass transport within the cell. More testing is required to obtain conclusive results.

The FESEM imaging was very beneficial. Though the fabrication techniques were identical, the PTFE- and Nafion-treated electrodes looked quite different. For a more accurate comparison between the two binders and how they affect the performance of a Li-O₂ battery, the electrode fabrication techniques should be improved, exploring unique incorporation protocols for each binder. Consulting PEMFC literature, where Nafion has been used as a binder for decades, may provide valuable insights.

CHAPTER 3
1D LI-O₂ BATTERY MODEL

3.1 Introduction

Theoretical modeling provides insights into the actual physical chemistry response of the battery to variations in the binder type (e.g., non-conductive PTFE vs. ion-conducting Nafion). What is transport like when Nafion is present? How does Nafion affect the battery chemistry? Of course, there is some missing information needed to truly model the behavior of Nafion within a functional Li-O₂ battery to answer these questions. The experiments mentioned in Chapter 2 begin to give us some of the required information. Additional experiments will lead to improvements in accuracy for current Li-O₂ theoretical modeling. This chapter describes the framework, results and discussion of our Li-O₂ model.

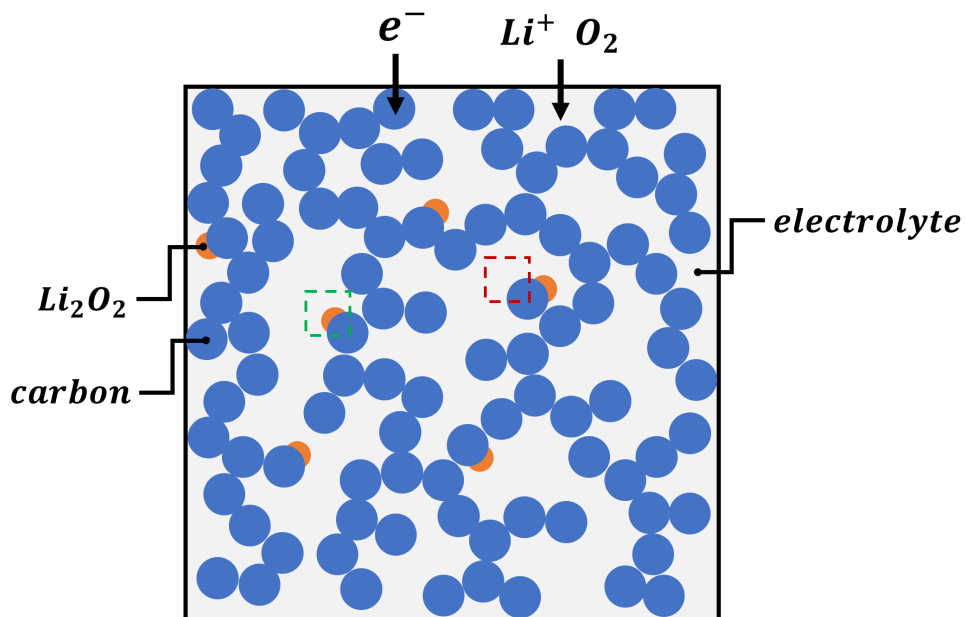


Figure 3.1: Theoretical model domain.

The 1D model presented below represents a Li-O₂ battery half-cell with a constant, user-defined current [18]. The model domain is given in Figure 3.1 and accounts for the

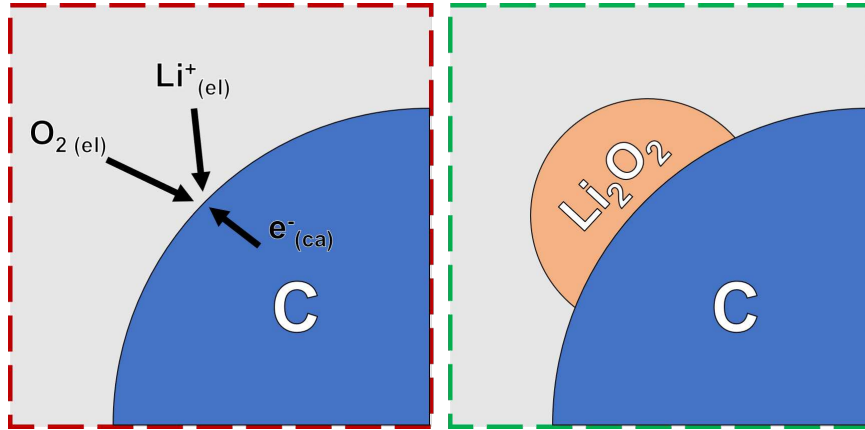


Figure 3.2: Li_2O_2 formation.

entire cathode of a Li- O_2 battery, with boundary conditions at the air/electrolyte and electrolyte/separator interfaces. The model has an initial volume fraction of carbon particles, electrolyte, binder and Li_2O_2 . Dissolved species such as Li^+ and O_2 move throughout the electrolyte, and the electrons move via the network of carbon particles. Before simulation, the cathode contains only electrolyte, carbon particles and binder (if applicable). Upon discharging, external current is removed to the cathode, as specified by the user input, which promotes the electrochemical reduction of the O_2 dissolved in the electrolyte to form bulk Li_2O_2 , which precipitates on the surface of the carbon particles, as in Figure 3.2. It is assumed the volume fraction of the carbon particles and binder remain constant throughout each simulation. Formation of bulk Li_2O_2 affects the available carbon surface area and concentration of the electrolyte species. The rate of the formation is dependent upon reaction kinetics, transport through the electrolyte and available carbon surface area at the given timestep. The simulation ends when Li_2O_2 is covering all available carbon or blocking pathways for further Li^+ or O_2 from accessing available surface area. This is an isothermal model, and it assumes instantaneous transport of electrons through the conductive carbon (i.e. the carbon is isopotential). At the air/electrolyte interface, only O_2 enters the electrolyte.

The model is written in Python and utilizes Cantera [19]. Cantera is an open source suite of tools that aids a model in calculating thermodynamic, kinetic and transport properties. A

Cantera input file (CTI) details specifics of the system being modeled (i.e. species, phases, interfaces, reactions) with the relevant thermodynamic and chemical kinetic property values. As the model runs, it supplies information about the state of the various battery phases (cathode, electrolyte, and Li_2O_2 precipitate in the cathode) to Cantera, and Cantera provides thermodynamic, kinetic and transport properties which are used to solve the governing equations of the model.

3.2 Model Framework

3.2.1 Governing equations

Three sets of differential variables define the state of the cathode at any given point in time: (1) the electrolyte electric potential (ϕ_{elyte}), (2) the volume fraction of Li_2O_2 in the cathode ($\epsilon_{\text{Li}_2\text{O}_2}$), and (3) the mass density of species within the available electrolyte volume ($\rho_{k,\text{elyte}}$). These variables are discretized spatially and then integrated over the specified simulation time, as dictated by three differential equations: (1) conservation of charge in the electrolyte, (2) conservation of mass of bulk Li_2O_2 in the cathode, and (3) conservation of mass of the electrolyte species.

Charge Neutrality Charge neutrality of the bulk electrolyte interior is implemented as Equation 3.1:

$$\sum [X_k]Z_k = 0, \quad (3.1)$$

where $[X_k]$ and Z_k are the concentration and elementary charge of species k , respectively.

Assuming the system is initially charge neutral, the derivative of the total charge with respect to time must also be zero as in Equation 3.2, for a given phase m .

$$\frac{\partial \sum [X_k]Z_k}{\partial t} = 0 \quad (3.2)$$

From conservation of charge, the derivative of total charge is also equal to the sum of all currents into and out of the electrolyte phase:

$$\frac{\partial \sum [X_k]Z_k}{\partial t} = \sum I|_m = 0 \quad (3.3)$$

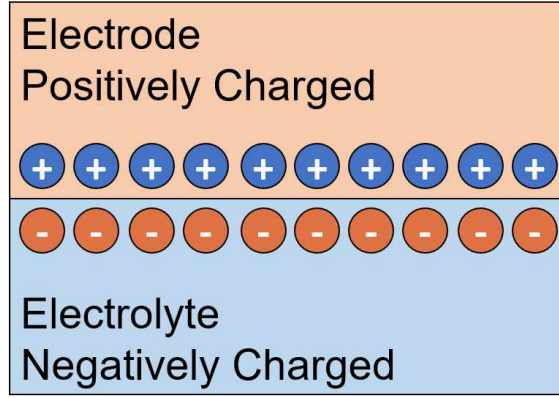


Figure 3.3: The double layer is the build-up of negative and positive charge at the interface of two phases.

Currents I could include electronic currents within the electrode phase, ionic currents within the electrolyte phase, or Faradaic current from charge-transfer at the interface of electrode and electrolyte phases. The sum of these currents is not necessarily equal to zero. Any excess charge must reside at the interface in the so-called charged double layer as in Figure 3.3. Any unbalanced charge transfer reactions will contribute to charging the double layer to maintain charge neutrality within the bulk interior. The charge neutrality condition becomes Equation 3.4.

$$I_{dl} = -I_{m,j-} + I_{m,j+} - I_{Far,j+} \quad (3.4)$$

where m represents the electronic or ionic phase current, and $j-$ and $j+$ represent the control volume boundaries toward and away from the origin, respectively. The charged double layer is capacitive. Its derivative can be written as Equation 3.5.

$$\frac{\partial \Delta \phi}{\partial t} = \frac{I_{dl}}{C_{dl}} \quad (3.5)$$

where C_{dl} is the double layer capacitance. In this model, the double layer capacitance changes with time based on Equation 3.6, where i_{dl} is double layer current per area, and A_{carb} is the interface area between electrolyte and carbon particle. The double layer current per area is calculated via Equation 3.7, and the Faradaic current i_{Far} is calculated in Equation

3.8.

$$\frac{\partial \Delta \phi}{\partial t} = \frac{i_{dl}}{C_{dl} A_{carb}} \quad (3.6)$$

$$i_{dl} = \nabla i_{io} + i_{Far} \quad (3.7)$$

$$i_{Far} = \dot{s}_{int,e} F \quad (3.8)$$

In Equation 3.8, $\dot{s}_{int,e}$ is the net production rate of electrons due to reactions at the carbon-electrolyte interface, and F is Faraday's constant. The double layer potential can be calculated as in Equation 3.9.

$$\Delta \phi = \phi_{carb} - \phi_{elyte} \quad (3.9)$$

Setting either the carbon potential ϕ_{carb} or electrolyte potential ϕ_{elyte} to zero gives a method for calculating the other potential. In this model, ϕ_{carb} is assumed to be zero, and ϕ_{elyte} is equal to the negative of the double layer potential $\Delta \phi$.

Interfacial area is a key variable in a Li-O₂ battery. The amount of available area at the carbon-electrolyte interface within the GDL is an indication of the state of charge of the battery. The volume fraction of the oxide forming upon discharge (Li₂O₂) is therefore also tracked in the model as per Equation 3.10. The volume fraction gives a method for determining how much Li₂O₂ has accumulated at each time step and the available surface area (i.e. surface area between carbon and electrolyte, not covered by Li₂O₂). In Equation 3.10, \dot{s}_{int,Li_2O_2} is the net production rate of the Li₂O₂, and V''' is the molar volume of Li₂O₂ in m³/kmol.

$$\frac{\partial \epsilon_{Li_2O_2}}{\partial t} = V''' \dot{s}_{int,Li_2O_2} \quad (3.10)$$

Within the model, the available surface area A_{carb} changes based on the volume fraction of the Li₂O₂ $\epsilon_{Li_2O_2}$ given by Equation 3.11. The new available surface area subtracts the area of the circle formed by the Li₂O₂ bulk hemisphere on the carbon from the initial available

surface area without any Li_2O_2 present in the cathode.

$$A_{carb} = A_{carb,init} - \frac{\frac{3}{2}\epsilon_{\text{Li}_2\text{O}_2}}{r_{\text{Li}_2\text{O}_2}} \quad (3.11)$$

Electrolyte conservation of mass is given in Equation 3.12, where N_k is the molar flux across node boundaries, W_{elyte} is a vector with all electrolyte species' molecular weights, ϵ_{elyte} is the electrolyte volume fraction in the porous carbon GDL, and \dot{s}_{surf} is the production rate of electrolyte species at the carbon/electrolyte interface. As described above, ions move between the double layer and electrolyte to preserve charge neutrality in the electrolyte. As such, \dot{s}_{surf} can be broken into two separate production rates $\dot{s}_{int,elyte}$ and \dot{s}_{dl} . Without loss of generality, we assume that the charge transfer between the double layer and electrolyte occurs exclusively due to the movement of Li^+ ions, and that the counter-ion does not contribute to the double-layer current. Thus, \dot{s}_{dl} is given in Equation 3.13, where \dot{s}_{dl} is a vector of all zeros with length equal to the number of electrolyte species, excluding the location corresponding to the Li^+ ion. With this division of production rates, the governing equation for conservation of mass becomes Equation 3.14.

$$\frac{\partial \rho_{k,elyte}}{\partial t} = \nabla N_k + \dot{s}_{surf} \frac{W_{elyte}}{\epsilon_{elyte}} \quad (3.12)$$

$$\dot{s}_{dl, \text{Li}^+} = \frac{i_{dl}}{F Z_{\text{Li}^+}} \quad (3.13)$$

$$\frac{\partial \rho_{k,elyte}}{\partial t} = \nabla N_k + (\dot{s}_{int,elyte} + \dot{s}_{dl}) \frac{W_{elyte}}{\epsilon_{elyte}} \quad (3.14)$$

3.2.2 Chemical and flux terms

The molar flux N_k in/out of a given node is driven by concentration and potential gradients between the current and adjacent nodes given in Equation 3.15, where $D_{k,elyte}$ is the concentration-driven diffusion coefficient, C_k is the concentration of each electrolyte species, $D_{k,mig}$ is the migration diffusion coefficient, ϕ_{elyte} is the potential of a node, ϵ_{elyte} is the volume fraction of the electrolyte, and brugg is the Bruggman coefficient.

$$N_k = -(D_{k,elyte} \nabla C_k + D_{k,mig} \nabla \phi_{elyte}) \epsilon_{elyte}^{\text{brugg}} \quad (3.15)$$

The two diffusion coefficients are calculated using an external function containing concentrated solution theory (CST). The external function receives system properties at the given time step to determine the coefficients. The ionic current i_{io} in/out of the node is given by Equation 3.16, where Z_k is a vector of the elementary charges of the electrolyte species.

$$i_{io} = \sum Z_k F N_k \quad (3.16)$$

3.2.3 Electrochemical kinetics

Forward and reverse reaction rate coefficients are given in Equations 3.17 and 3.18, respectively.

$$k_f = k_f^* \exp\left(-\frac{\beta n F \Delta\phi}{RT}\right) \quad (3.17)$$

$$k_r = k_r^* \exp\left(\frac{(1 - \beta) n F \Delta\phi}{RT}\right) \quad (3.18)$$

In these equations, k_f^* and k_r^* are the standard chemical reaction rate coefficients, calculated according to the Arrhenius parameters for a given species j in Equation 3.19.

$$k_j^* = A_j T^{n,j} \exp\left(-\frac{E_{act,j}}{RT}\right) \quad (3.19)$$

where A_j reflects the steric, collision rate and other effects, n captures temperature dependence, and E_{act} represents the activation barrier.

3.2.4 Boundary conditions

Figure 3.4 gives the transport equations at the boundaries and interior nodes. At the gas channel/GDL interface, the electronic current i_{el} is the prescribed external current i_{ext} , and the ionic current i_{io} is zero. The molar flux into the GDL is given by a net production rate for O_2 transferring from the gas to electrolyte phase. At the GDL/separator interface, there is no electronic current i_{el} , and to preserve charge neutrality, the ionic current i_{io} is set as the prescribed external current i_{ext} . The Li^+ ion is assumed to be the only flux at this

boundary and its molar flux is given by Equation 3.20.

$$N_{Li^+} = \frac{i_{io}}{F Z_{Li^+}} \quad (3.20)$$

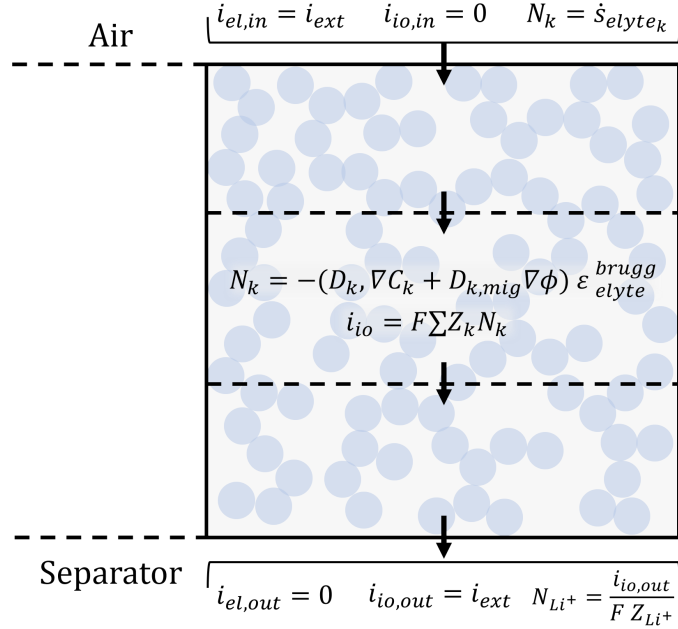


Figure 3.4: Current and molar flux within the GDL, with boundary conditions at the air and separator interfaces.

3.3 Binder Effects

This half-cell model is used to evaluate the difference in performance between Li-O₂ cells containing non-conductive (PTFE) and conductive (Nafion) binders. To make this comparison, the approximate volume fraction of binder in a typical cell is determined by optical evaluation of SEM images of an electrode containing PTFE (Figure 3.3). The image was split up into a fine, square grid. Each individual square was assigned a binary value. Squares with visible open space were assigned 0, and squares containing mostly solid material were assigned 1. The total volume fraction of solid material was calculated as the number of squares assigned as 1 divided by the total number of squares. The amount of solid material represents the total volume fraction of binder and carbon paper. From manufacturer specifications, the carbon paper has a volume fraction of 20% carbon, therefore the volume

fraction of the binder is calculated as the carbon volume fraction subtracted from the total volume fraction of solid material. This binder volume fraction ϵ_{binder} affects 3 other variables within the model: the available surface area A_{int} , volume fraction of solid materials ϵ_{solid} (carbon and binder), and the initial electrolyte volume fraction ϵ_{elyte} (volume excluding solid material). The binder volume fraction is incorporated into the interface area as per Equation 3.21, where A_{part} and V_{part} are the area and volume of a single carbon particle, respectively [20].

$$A_{carb} = \epsilon_{carb}(1 - \epsilon_{binder}) \frac{A_{part}}{V_{part}} \quad (3.21)$$

A non-conductive binder, such as PTFE, prevents Li^+ ions and O_2 molecules from passing through it to reach the electrons at the carbon surface to form Li_2O_2 . The binder, therefore, reduces the available surface area in the cathode. Nafion, a conductive binder, allows for Li^+ and O_2 to pass through. If sufficiently conductive, the Nafion could allow for Li_2O_2 to form on areas other than exposed carbon (i.e. on Nafion’s surface, or at the Nafion-carbon interface), effectively increasing the available surface area and lessening the effect on transport of ions through the cathode. Though the Nafion and PTFE occupy the same amount of physical space within the cathode, the Nafion effectively has a smaller volume because it has a smaller impact on the interface area A_{carb} and cathode porosity ($\epsilon_{carb} + \epsilon_{binder}$). For this reason, the binder volume fraction for the Nafion cell was treated as an “effective volume fraction” to capture the influence of Nafion’s conductivity and behavior in a Li- O_2 battery. The effective volume fraction will be fitted to experimental data taken from a cell containing Nafion. Comparing this effective volume fraction of the PTFE and Nafion cells will give a quantitative method for measuring the improvement in cell performance from a conductive binder.

3.4 Model Fitting and Validation

The model was validated using discharge capacity versus cycle number data from cells containing PTFE and Nafion, as shown in Figure 3.6. The PTFE fit used the 0.52 binder

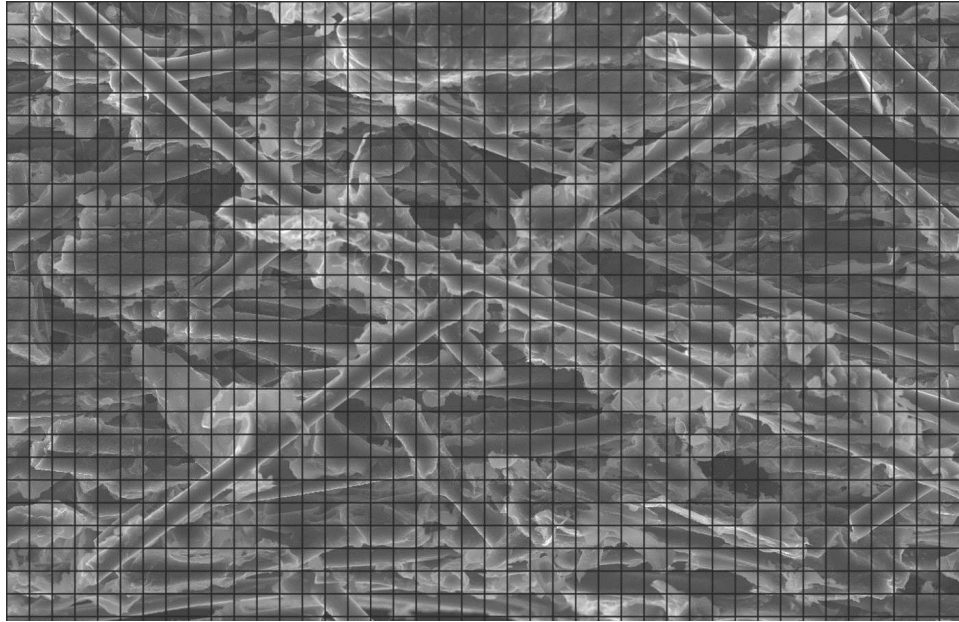


Figure 3.5: Image used to determine the volume fraction of binder in a PTFE electrode.

volume fraction based on Figure 3.5, with an R^2 value of 0.52. The effective volume fraction that provided the best fit to the Nafion data was 0.43, with an R^2 value of 0.94.

The shape of the charge curves from the experiments (Figure 2.4) indicate the battery is not being fully charged, and some Li_2O_2 is left in the cathode. To mimic this effect, a “short-charge” factor of 0.9 was multiplied by the time required to fully charge/discharge the battery. Though the model lacks the physics that would capture degradation effects due to harmful side reactions, etc., the model fits the curve in the data almost exactly with the addition of the short-charge factor.

3.5 Results

The following figures investigate the variations of certain model parameters with cathode depth at various states of discharge. The legend entries represent discharge capacity at the given timestep.

The available surface area A_{carb} , electrolyte volume fraction ϵ_{elyte} and Li_2O_2 volume fraction $\epsilon_{\text{Li}_2\text{O}_2}$ all vary with capacity, as in Figure 3.7, Figure 3.8 and Figure 3.9, respectively.

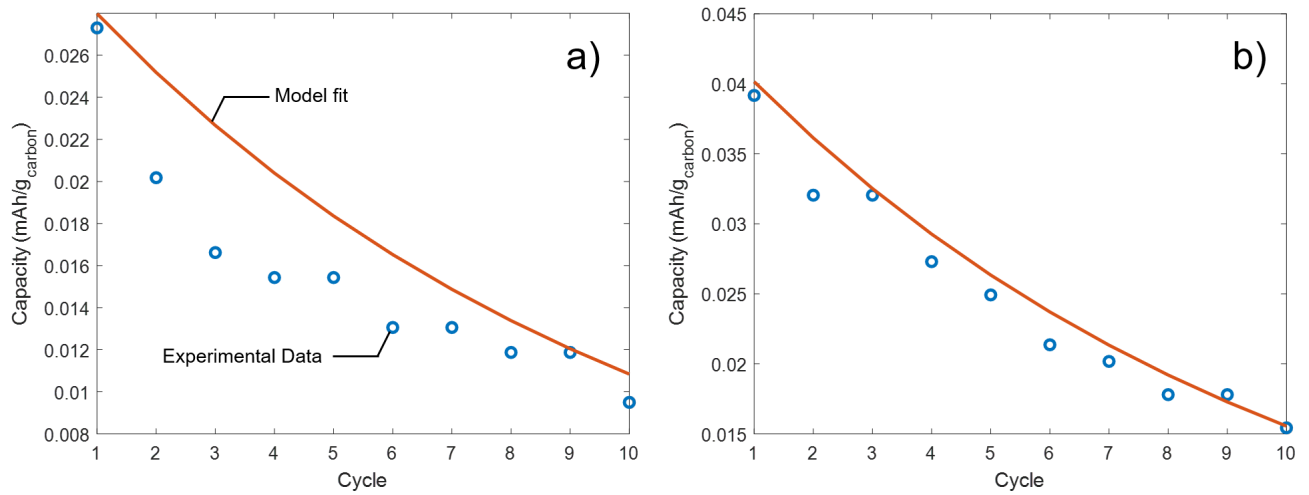


Figure 3.6: Experimental data and model fit of discharge capacity versus cycle for (a) PTFE-treated cell and (b) Nafion-treated cell.

The three variables also differ between PTFE and Nafion cells. The available surface area for the Nafion cell is higher than in the PTFE cell by about $10,000 \text{ m}^2$ before discharging and remains higher as the battery is discharged. Additionally, $\epsilon_{Li_2O_2}$ is higher in the Nafion cell, likely due to the increased A_{carb} . More surface area allows for more Li_2O_2 to be formed, resulting in a higher $\epsilon_{Li_2O_2}$.

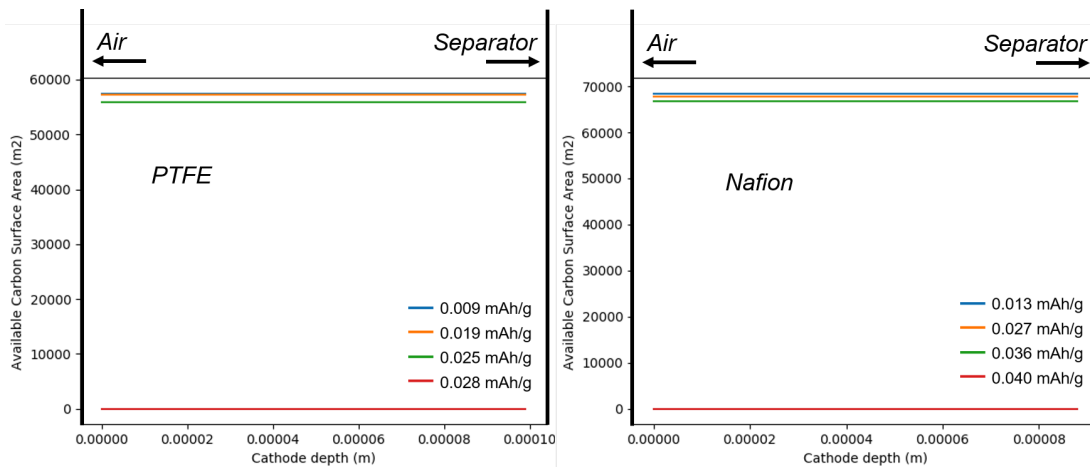


Figure 3.7: Available carbon surface area versus cathode depth.

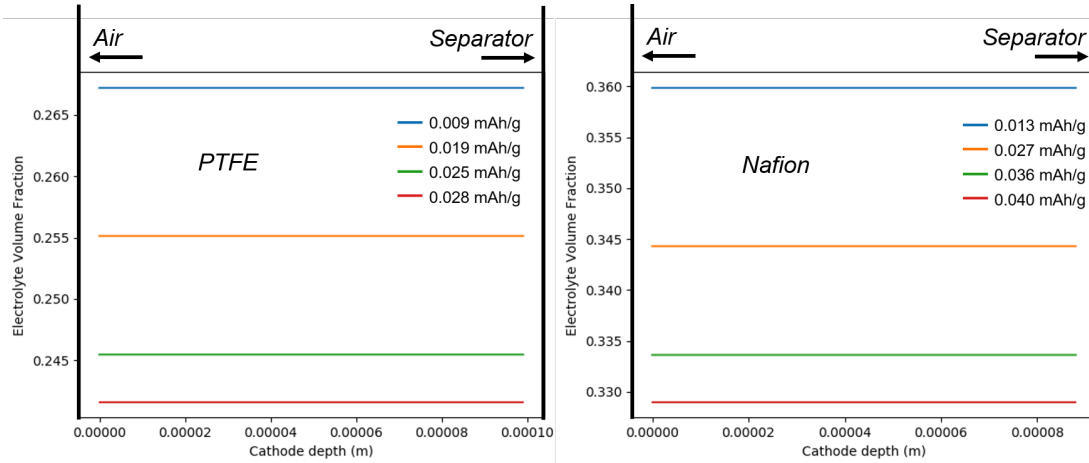


Figure 3.8: Electrolyte volume fraction versus cathode depth.

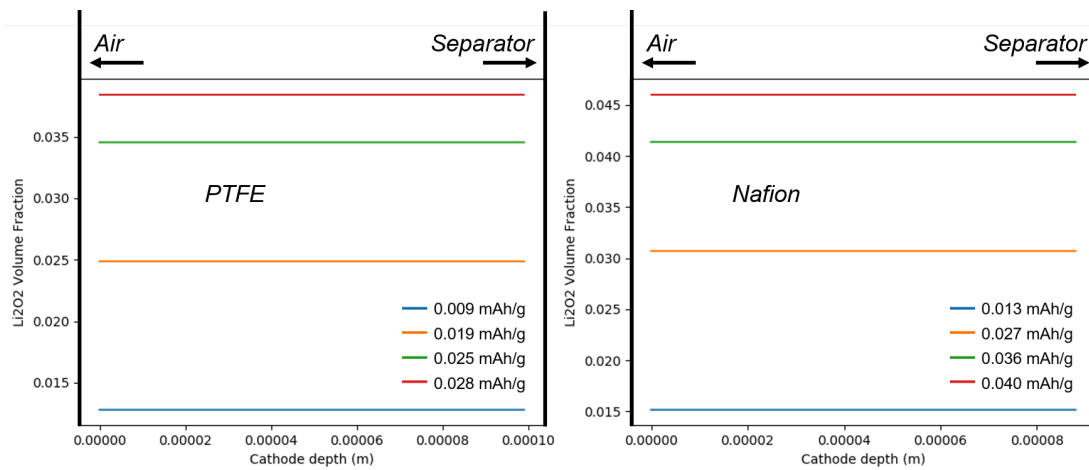


Figure 3.9: Li₂O₂ volume fraction versus cathode depth.

The Li^+ and O_2 concentrations do not show a significant variation with cathode depth. However, at small scales, there is a trend that emerges. The O_2 concentration (Figure 3.10) decreases with cathode depth. The air/electrolyte interface is at a cathode depth of zero. Further from that interface, there is less O_2 . The same is true for the Li^+ concentration (Figure 3.11). Higher cathode depth values have a higher Li^+ concentration. Unlike the plot of the O_2 concentration, the order of the capacities changes depending on the cathode depth. For instance, the Li^+ concentration is highest at the highest capacity at the electrolyte/separator interface. At the air/electrolyte interface, the Li^+ concentration is at its lowest at that same highest capacity.

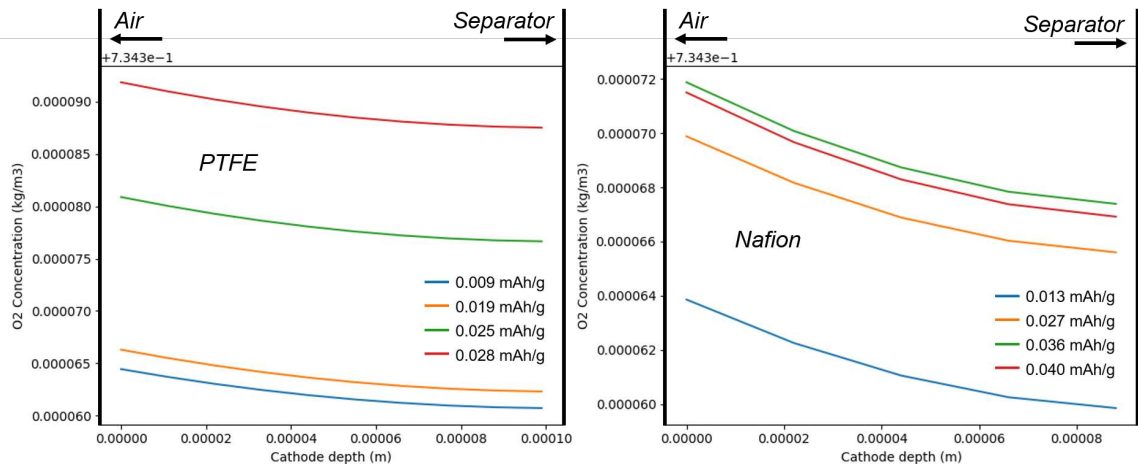


Figure 3.10: O_2 concentration versus cathode depth

3.6 Discussion

The model confirms that surface area plays a notable role in Li- O_2 batteries. In the model, the increased available surface area in the Nafion cell proves to be responsible for the increase in discharge capacity in a cell containing Nafion versus PTFE. The simulations stop when A_{carb} is zero, indicating the surface area is the limiting factor in this Li- O_2 battery model. The effective volume fraction for the binder in the Nafion cell is 20% lower than in the PTFE cell – though the two polymers occupy the same physical space within the cathode, the cell with a Nafion binder can store more Li_2O_2 than with PTFE. Though the

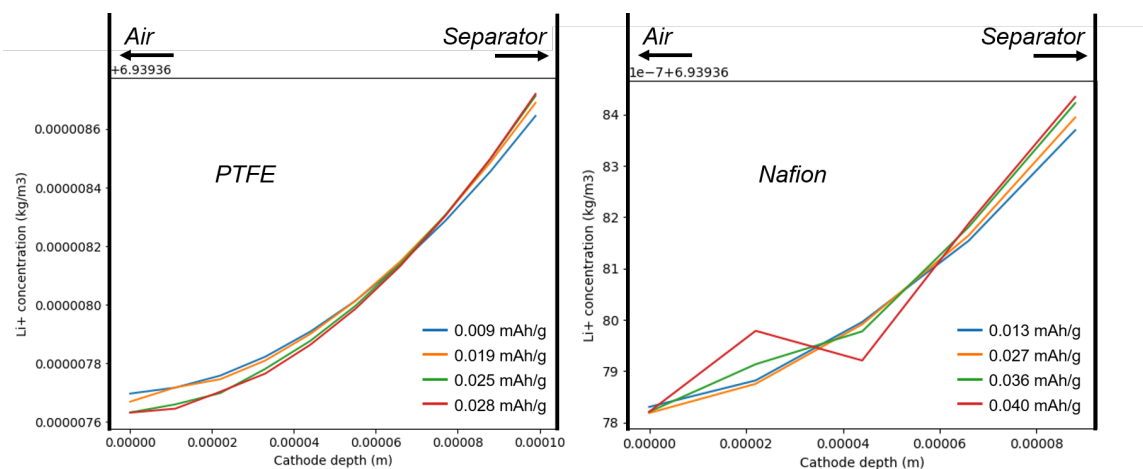


Figure 3.11: Li^+ concentration versus cathode depth

model does not account for binder properties such as conductivity, a Nafion binder has an obvious effect on how much Li_2O_2 can form.

The capacity degradation seen in the experimental data is captured in the “short-charge” factor, indicating that much of that apparent “degradation” is due to the residual Li_2O_2 left after an incomplete charge. As discussed in Chapter 2, this incomplete charge is a result of large overpotentials during charging, which suggest that the cutoff voltage (dictated, in turn, by rather conservative thermodynamic stability limits) was reached before charging was complete. A longer charge time would likely improve the capacity of $\text{Li}-\text{O}_2$ batteries with both PTFE and Nafion binders but would also likely result in deleterious side reactions at the cathode/electrolyte interface (e.g., electrolyte reduction). This is not to say that the short-charge effect is the only factor in capacity degradation, as there are many physical parameters excluded from this model that could play a significant role in the capacity reduction, such as formation of Li_2CO_3 or degradation of the lithium anode [21].

There was no variation in the model parameters with cathode depth. At small scales, there was a slight change in the O_2 and Li^+ concentrations depending on the location in the cathode, though the change did not affect the reaction as all other parameters did not show dependence on cathode depth. At higher charge rates, transport may become a limiting

factor in battery capacity as the reactions are driven at faster rates.

3.7 Conclusions

The results from this model are promising and give good cause to continue to investigate Nafion as a replacement for PTFE in Li-O₂ batteries. Based on the results from this model, Nafion impacts the battery performance by increasing the available surface area, allowing more Li₂O₂ to form. At the low charge rate run in the simulations, there are noted variations in Li⁺ and O₂ concentrations throughout the cathode. As the model is pushed to higher charge rates, these variations may become limiting.

Further efforts toward the expansion and refinement of this model may include the incorporation of relevant physics. Understanding the physical phenomena of binder conductivity may aid in the understanding of how Nafion is able to effectively increase the available surface area in the cathode. Additionally, the increased information gained from higher resolution SEM and the incorporation of backscattered electron images (in addition to the secondary electron images presented) could allow for increased understanding of how to model the binder as model fidelity increases.

CHAPTER 4

CONCLUSIONS

Li-O₂ batteries have the potential to enable electric vehicles with longer driving ranges. Their theoretical energy density is much higher than current Li-ion battery technology allows. There are limitations associated with Li-O₂ batteries that have kept the technology from reaching the theoretical limit. One such limitation involves the binder's conductivity. The most commonly used binder in Li-O₂ batteries is PTFE. PTFE is a non-conductive polymer, meaning transport through the material is severely limited and reduces the capacity of the battery. This study explored the effects of a conductive polymer binder, such as Nafion, on Li-O₂ battery performance.

The experiments provided preliminary results for the overarching DOE-funded project on active-polymer. The modeling efforts in this study simulated a Li-O₂ half-cell undergoing a constant-current charge/discharge process and investigated the differences between Nafion and PTFE within the cell.

4.1 Summary of Efforts

Electrochemical experiments were conducted to compare the performance of a Li-O₂ battery cell containing PTFE and Nafion. Testing set-up and protocols were developed over the course of 6 months to ensure consistent and accurate electrochemical testing results. The test set-up allows for up to two inlet gases to enter the cell and contains an outlet port for possible gas analysis, such as mass spectrometry. Cycling and EIS data were used to analyze the cell performance.

A half-cell theoretical model was developed to simulate the behavior of a Li-O₂ battery with both a PTFE and Nafion binder, and was fit to the experimental data. Model fitting to the experiments with cells containing Nafion was used to compare the behavior of both

binders from an internal point-of-view. The effects of the binder on available surface area and porosity within the cathode are used as metrics to compare the two.

FESEM imaging was used to investigate the qualitative impact of the binders on the structure of the cathode. These images impacted cathode fabrication techniques, as well as model parameters.

4.2 Key Findings

The results from the Li-O₂ cell experiments were largely inconclusive. The first round of testing showed an improvement in discharge capacity with the addition of a Nafion binder. However, the repeated experiments showed the opposite results. EIS taken with the first round of testing gave some indication as to why the Nafion cell had higher capacity - it had lower resistances and higher Warburg impedances, indicating better mass transport within the cell. More testing is required to obtain conclusive results.

FESEM imaging provided a method with which to make a visual comparison between electrodes considered in this study. The images proved Nafion and PTFE require separate processes when being incorporated in carbon paper. The microstructures of the two electrodes were very different – there was significant agglomeration of Nafion in certain sections of the carbon paper, while the PTFE appeared well-dispersed throughout. These differences and inconsistencies could be to blame for the inconclusive discharge capacity results between trials. The two binders were added to the carbon paper using the same protocol, but different microstructures were produced. A separate protocol must be developed for each of the binders to produce similar binder loading and microstructure between them. Applying a potential to the Nafion binder solution could improve the molecular dispersion.

There is a possibility that the Nafion electrode fabrication process was inconsistent to the point that the improvement in capacity and impedances in the Nafion cells was due to the bare carbon fibers rather than the conductivity of the Nafion itself. As SEM imaging showed, there is an obvious separation between where the bulk of the Nafion is located and the carbon fibers. The improved performance in the first round of testing could be due to

the exposed carbon fibers, where the reaction to form Li_2O_2 is not impeded by a binder. However, there was assumed to be equal binder loading between the Nafion and PTFE cases. If Nafion simply had a different microstructure with large agglomerates, this might hinder transport. On the contrary, there was a performance improvement with the Nafion binder in round one of testing, indicating the ionic conductivity of Nafion did have a benefit with respect to transport. These inconsistencies need to be addressed with further work in order to improve repeatability with the experiments.

The polymeric structural differences between the two polymers may be relevant as well – Nafion’s side chain could be promoting the agglomeration seen in the images. Improved dispersion of the Nafion could further improve the battery performance, as the cathode microstructure would contain more consistent pore space for species transport.

The model suggests the limiting factor in a Li- O_2 battery cathode is surface area. Nafion effectively increases the available surface area for Li_2O_2 to form, and thus results in a higher discharge capacity. The conductivity of Nafion could allow Li_2O_2 to form on surfaces other than those at the carbon/electrolyte interface. For instance, if the sufficiently conductive, Li^+ ions and O_2 could travel through the Nafion to the carbon/binder interface and react to form Li_2O_2 at that interface. A Nafion binder does not restrict Li_2O_2 formation to the carbon/electrolyte interface.

The model also captures some transport phenomena. Nafion’s effective volume fraction is smaller than PTFE’s, and therefore the space for species to move through the electrolyte is larger in a Nafion cell. Both increased surface area and improved transport contribute to Nafion’s improved capacity.

4.3 Future Work

Current FESEM images of the binder coatings showed improvements are necessary for future, more successful Li- O_2 cathodes. The binder loading in the current cathodes was inconsistent. A microstructure similar to the Toray paper (Figure Figure 2.13) would provide improved transport and even Li_2O_2 formation throughout the cathode. Methods to

make the PTFE and Nafion binder coatings more consistent would give a more accurate comparison between the two and can improve experimental repeatability. More advanced characterization techniques, such as energy dispersive spectroscopy (EDS), would provide compositional information about the cathode before and after cycling. This data would help not only with improving the electrode fabrication process, but also in improving the model approach. Information about the composition of the electrode after charging would be especially helpful in identifying the formation of certain unwanted species, such as Li_2CO_3 , that degrade and passivate the battery. The formation of such substances could be incorporated into the model and better capture battery degradation effects.

The experimental results presented in this study included two trials of each cathode type. Though the discharge capacity results of the two trials were on the same order of magnitude, there was not perfect agreement. Future experiments should be run to ensure repeatability of the results presented in this study.

Carbon paper without a binder provided the highest discharge capacity in the experiments. The carbon paper used gives a low surface area cell. Traditionally, binders are necessary for electrodes containing carbon particles, such as carbon black. The binder maintains a structure in the carbon particles and binds them together. The impacts of the two binders within a high-capacity battery should be evaluated, such as with carbon particles, rather than fibers, to truly test the impact of a conductive polymer binder. This would also bring the cell capacity closer to the theoretical limit.

The current model shows that a Nafion binder effectively increases the carbon surface area within a Li-O₂ battery cathode, but the reason for this is not known. Is the improvement due to Nafion's conductivity alone? Are there other factors such as interactions between the binder and electrolyte that are at play? Including more physics within the model such as binder conductivities, degradation effects and reverse reaction mechanisms could improve the understanding of Nafion's behavior and answer some of these questions. Additionally, converting the model from half-cell to full-cell would help capture effects of the separator

and anode that could contribute to performance differences. Subjecting the battery model to different charging conditions, such as fast-charging, would also give a more comprehensive view of Nafion's behavior.

4.4 Outlook

Though the results from this study could not conclusively determine whether a Nafion binder improves Li-O₂ battery performance, Nafion should continue to be investigated as a replacement for a PTFE binder. Inconsistencies in binder loading may play a notable role in the performance of the battery. Improved binder electrode fabrication processes will give more definitive comparison between the two binders.

Binders are not necessary for electrodes in which the carbon already has a coherent structure, as in the cathodes used in this study. Cathodes comprised of carbon particles like carbon black require a binder to maintain their structure and to ensure a conductive pathway for electrons. The particles also increase the carbon surface area. With the addition of carbon particles, we expect to see an even larger increase in the capacity, bringing Li-O₂ batteries one step closer to becoming commercially viable.

REFERENCES CITED

- [1] D. G. Kwabi et al. Materials challenges in rechargeable lithium-air batteries. *MRS Bull.*, 39(5):443–452, 2014.
- [2] M. Han H. Jung, R. Silva. Scaling trends of electric vehicle performance: Driving range, fuel economy, peak power output, and temperature effect. *World Electr. Veh. J.*, 9(4): 46, 2018.
- [3] B. D. Adams et al. Towards a stable organic electrolyte for the lithium oxygen battery. *Adv. Energy Mater.*, 5(1):1–11, 2015.
- [4] Y. Chen Z. Peng, S. A. Freunberger and P. G. Bruce. A reversible and higher-rate li-o2 battery. *Science*, 337(6094):563–566, 2012.
- [5] Z. Peng Y. Chen Z. Liu M. M. Ottakam Thotiyl, S. A. Freunberger and P. G. Bruce. A stable cathode for the aprotic li-o2 battery. *Nat. Mater.*, 12(11):1050–1056, 2013.
- [6] H. Beyer J. Schwammlein S. Meini, M. Piana and H. A. Gasteiger. Effect of carbon surface area on first discharge capacity of li-o2 cathodes and cycle-life behavior in ether-based electrolytes. *J. Electrochem. Soc.*, 159(12):A2135–A2142, 2012.
- [7] M. Augustin D. Fenske A. Wittstock I. Bardenhagen, O. Yezerska and M. Bäumer. In situ investigation of pore clogging during discharge of a li/o2 battery by electrochemical impedance spectroscopy. *J. Power Sources*, 2015.
- [8] Z. Peng M. M. Ottakam Thotiyl, S. A. Freunberger and P. G. Bruce. The carbon electrode in nonaqueous li-o2 cells. *J. Am. Chem. Soc.*, 135(1):494–500, 2015.
- [9] C. Francia S. Bodoardo J. Zeng, J. R. Nair and N. Penazzi. Aprotic li-o 2 cells: Gas diffusion layer (gdl) as catalyst free cathode and tetraglyme/liclo 4 as electrolyte. *Solid State Ionics*, 262:160–164, 2014.
- [10] Y. Shao-Horn C. V. Amanchukwu, J. R. Harding and P. T. Hammond. Understanding the chemical stability of polymers for lithium-air batteries. *Chem. Mater.*, 27(2):550–561, 2015.
- [11] M. H. Engelhard Z. Nie X. S. Li E. Nasybulin, W. Xu and J. G. Zhang. Stability of polymer binders in li-o2 batteries. *J. Power Sources*, 243:899–907, 2013.

- [12] H. Cheng and K. Scott. Improving performance of rechargeable li-air batteries from using li-nafion® binder. *Electrochim. Acta*, 116:51–58, 2014.
- [13] S. C. Decaluwe. Flow-through neutron reflectometry – an in operando sample environment for active polymer interface studies. 2013.
- [14] B. K. D. Bknd.
- [15] R. Nelson M. H. Weatherspoon J. Gomez, E. E. Kalu and J. P. Zheng. Binder-free co-mn composite oxide for li-air battery electrode. *Journal of Materials Chemistry A*, 1:3287–3294, 2013.
- [16] W. Weng et al. Polymer supported organic catalysts for o2 reduction in li-o2 batteries. *Electrochim. Acta*, 19:138–143, 2014.
- [17] Y. Chen Z. Peng, S. A. Freunberger and P. G. Bruce. A reversible and higher-rate li-o2 battery. *Science*, 337(6094).
- [18] CORES Research Group. Battery–cantera: Modeling fundamental physical chemistry in batteries using cantera. <https://github.com/coresresearch/BatCan>, 2019.
- [19] David G. Goodwin, Raymond L. Speth, Harry K. Moffat, and Bryan W. Weber. Cantera: An object-oriented software toolkit for chemical kinetics, thermodynamics, and transport processes. <https://www.cantera.org>, 2018. Version 2.4.0.
- [20] A. Torayev V. Thangavel Y. Yin, C. Gaya and A. A. Franco. Impact of li2o2 particle size on li-o2 battery charge process: Insights from a multiscale modeling perspective. *J. Phys. Chem. Lett*, 7(19).
- [21] M. Tokur H. Algül T. Çetinkaya A. Akbulut Uludag, H. Akbulut and M. Uysa. Stability effect of some organic and inorganic additions in the emitfsi-litfsi nanocomposite electrolytes for lithium-air batteries. *Microsyst. Technol.*, 22(5).

APPENDIX
CELL ASSEMBLY AND DISASSEMBLY

A.1 Electrolyte Preparation - 1 M LiTFSI in TEGDME

1. Measure 100 mL of TEGDME in a glass jar. Dry over 4 Å molecular sieves for 2 hours at 40 C. Vacuum dry at 80 C overnight. Move quickly to glovebox.
2. Measure 28.71 g of LiTFSI in beaker. Vacuum dry at 80 C overnight. Move quickly to glovebox.
3. In the glovebox, dissolve LiTFSI in TEGDME.

A.2 Cell Assembly

1. Dry carbon paper and glass fiber separator in vacuum furnace at 200 C overnight. Move quickly to glovebox.
2. Load the feed-through hole of the REF sleeve with a small amount of lithium metal using the REFloader.
 - Take care that the narrow part of the feed-through hole is *completely* filled with lithium, so that the lithium filling gets into direct contact with the separator inside the sleeve and with the REF pin from outside.
3. Insert the REF sleeve into the cell base.
4. Mount the locking washer, thereby aligning the side opening of the cell base with the feedthrough hole of the REF sleeve.
5. Attach the reference pin assembly to the cell base.
6. Place the working electrode (18 mm diameter carbon paper) into the sleeve on the spiral-type flow field.

7. Put the glass fiber separator on top of the working electrode.
8. Dispense 500 μL of electrolyte onto the separator.
9. Place a lithium metal disc (punched to 18 mm diameter) on top of the separator inside the sleeve.
10. Insert the plunger, the spring, and the PE seal.
11. Attach the cell lid, insert the cell into the bracket, and tighten the wing nut – ensure the lid is not touching the stand.
12. Close the ball valves at inlet and outlet gas tubes. Let cell rest in glovebox, sealed, for 6 hours.
13. Remove cell from glovebox and move quickly to fume hood. Connect the cell to the gas supply.
14. Purge O_2 tubing with dry O_2 before opening the valve to the cell inlet.

A.3 Disassembly and Cleaning

Right after use, disassemble the cell in the reverse order of assembly. Note that the reference pin MUST be detached before the REF sleeve can be removed.

1. Place all cell parts (base, plunger, spring, REF sleeve, lid) in a room temperature, ultrasonic bath of DI water for 1 hour.
2. Dry all parts with paper towel and let sit in air until completely dry.
3. Move the parts in the vacuum furnace and heat overnight at 80 C.
4. Move cell parts quickly to glove box for storage.

All chemicals used must be disposed of properly. The cell parts including the lid and the spring are to be cleaned in an ultrasonic bath with detergent wash. Persistent dirt on the

cell base and plunger may be removed by treating these parts with aqueous nitric acid (20%, 2 hours at room temperature). Afterwards, the parts are to be rinsed with water, and to be dried at 80 C. PE seals and PTFE ferrules are to be replaced.